Human neutrophils produce antifungal extracellular vesicles against *Aspergillus fumigatus*

Iordana A. Shopova[1,2], Ivan Belyaev[3,9], Prasad Dasari[4], Susanne Jahreis[5], Maria C. Stroe[1,2], Zoltán Cseresnyés[3], Ann-Kathrin Zimmermann[1,2], Anna Medyukhina[3], Carl-Magnus Svensson[3], Thomas Krüger[2], Viktória Szeifert[6], Sandor Nietzsche[7], Theresia Conrad[8], Matthew G. Blango[2], Olaf Kniemeyer[2], Marie von Lilienfeld-Toal[5], Peter F. Zipfel[1,4], Erzsébet Ligeti[6], Marc Thilo Figge[1,3], and Axel A. Brakhage[1,2*]

[1]Institute of Microbiology, Friedrich Schiller University, Jena, Germany

[2]Department of Molecular and Applied Microbiology, Leibniz Institute for Natural Product Research and Infection Biology (HKI), Jena, Germany

[3]Research Group Applied Systems Biology, Leibniz Institute for Natural Product Research and Infection Biology (HKI), Jena, Germany

[4]Department of Infection Biology, Leibniz Institute for Natural Product Research and Infection Biology (HKI), Jena, Germany

[5]Clinic of Internal Medicine II, Haematology and Oncology, Jena University Hospital, Jena, Germany,

[6]Department of Physiology, Semmelweis University, Budapest, Hungary,

[7]Centre for Electron Microscopy, Jena University Hospital, Jena, Germany

[8]Research Group Systems Biology and Bioinformatics, Leibniz Institute for Natural Product Research and Infection Biology (HKI), Jena, Germany

[9]Friedrich Schiller University, Jena, Germany

*Corresponding author:

Email: axel.brakhage@uni-jena.de (AAB)

Abstract

Polymorphonuclear granulocytes (PMNs) are indispensable for controlling life-threatening fungal infections. In addition to various effector mechanisms, PMNs also produce extracellular vesicles (EVs). Their contribution to antifungal defense has remained unexplored. We reveal that the clinically important human pathogenic fungus *Aspergillus fumigatus* triggers PMNs to release a distinct set of antifungal EVs (afEVs). Proteome analyses indicated that afEVs are enriched in antimicrobial proteins. The cargo and release kinetics of EVs are modulated by the fungal strain confronted. Tracking of afEVs indicated that they associated with fungal cells and even entered fungal hyphae, resulting in alterations in the morphology of the fungal cell wall and dose-dependent antifungal effects. Two human proteins enriched in afEVs, cathepsin G and azurocidin, were heterologously expressed in fungal hyphae, which led to reduced fungal growth relative to a control retinol binding protein 7 producing strain. In conclusion, the production of afEVs by PMNs offers an intriguing, previously overlooked mechanism of antifungal defense against *A. fumigatus*.

Importance

Invasive fungal infections caused by the mold *Aspergillus fumigatus* are a growing concern in the clinic due to the increasing use of immunosuppressive therapies and increasing antifungal drug resistance. These infections result in high mortality as treatment and diagnostic options remain limited. In healthy individuals, neutrophilic granulocytes are critical for elimination of *A. fumigatus* from the host; however, the exact extracellular mechanism of neutrophil-mediated antifungal activity remains unresolved. Here, we present a mode of antifungal defense employed by human

neutrophils against *A. fumigatus* not previously described. We find that extracellular vesicles produced by neutrophils in response to *A. fumigatus* infection are able to associate with the fungus, limit growth, and elicit cell damage by delivering antifungal cargo. In the end, antifungal extracellular vesicle biology provides a significant step forward in our understanding of *A. fumigatus* host pathogenesis and opens up novel diagnostic and therapeutic possibilities.

Introduction

Clinical management of invasive aspergillosis, a severe systemic infection mainly caused by the ubiquitous saprophytic fungus *Aspergillus fumigatus*, is a challenging endeavor. Invasive aspergillosis is characterized by high mortality rates related to difficult diagnosis, the occurrence of resistance to antifungals, and the lack of novel antifungal therapies (1-6). Invasive aspergillosis can occur in patients with congenital or therapy-induced myeloid cell defects, whereas healthy individuals that continuously inhale fungal spores (conidia; 2-3 µm), usually remain symptom-free. Data from neutropenic mice and patients have shown that polymorphonuclear granulocytes (PMNs) are indispensable for antifungal defense (7-16); however, the exact mechanism of PMN-dependent fungal killing remains unresolved.

PMNs orchestrate immune surveillance against pathogenic fungi *via* oxidative burst (14, 17, 18), degranulation (19, 20), phagocytosis (21), cytokine release (7), and extracellular trap formation (11, 16, 22, 23). Neutrophil extracellular traps are only slightly fungistatic, and this alone does not explain the full antifungal activity of PMNs (22, 23). In addition to these effector mechanisms, PMNs also produce PMN-derived extracellular vesicles, which represent extracellular phosphatidylserine-containing microparticles (50 nm to 1 µm) that elicit pleiotropic immunomodulatory effects in recipient host cells (24-28). PMN-derived EVs serve many functions *in vivo*

(29-32) including antibacterial (33-35) and antiviral (36) defense and have been used as diagnostic markers for sepsis (37). Previous work also indicated that opsonization of bacteria was required for production of PMN-derived EVs (34).

In this manuscript, we demonstrate the immune functionality of PMN-derived EVs against the important filamentous fungal pathogen *A. fumigatus*. We phenotypically characterize the EVs produced by PMNs in response to *A. fumigatus* infection and further detail the properties, locations, and antifungal effects of these EVs on the fungus.

Results

PMNs release EVs in response to *A. fumigatus* infection

Confrontation of PMNs with *A. fumigatus* conidia is known to result in rapid internalization of the fungus and production of reactive oxygen intermediates and neutrophil extracellular traps over time (38, 39), yet the role of EVs in antifungal defense remains unexplored. As such, we enriched and characterized PMN-derived EVs produced from viable PMNs (>95% purity, >98% viability) during infection with opsonized wild-type (wt) *A. fumigatus* conidia (Fig. S1A). To limit PMN apoptosis and subsequent production of apoptotic bodies, we first determined the apoptotic fate of PMNs over the course of interaction with *A. fumigatus* by monitoring propidium iodide (PI) and Annexin V staining of cells using flow cytometry (Fig. 1A). Apoptotic cells expose phosphatidylserine on the outer leaflet of the cell membrane during early apoptosis and also become permeable to PI at later stages of apoptosis. By size discrimination using flow cytometry, we could also distinguish between cellular apoptosis and the release of apoptotic bodies (Annexin V^+/PI^+ EVs) (Fig. 1A and Fig. S1B-E). Coincubation of human PMNs with fungi for 4 h, at a multiplicity of infection (MOI) of 5 conidia to 1 PMN, triggered minimal cell death in the PMN population

(<10%) and limited apoptotic body release compared to an MOI of 10 (Fig. 1A). An MOI of 5 was thus used throughout the remainder of the study to phenotypically characterize PMN-derived EVs.

We were particularly interested in the phosphatidylserine-containing and PI-negative fraction of EVs linked to host immunity previously described in the literature, which could be interrogated by flow cytometry (24-28). Labeling of EVs with cell surface markers for the α-chain of the integrin receptor CR3 (CD11b) and the tetraspanin CD63 revealed an increase in the populations of antifungal EVs (afEVs) produced in response to infection with wt *A. fumigatus* relative to spontaneously released EVs from uninfected cells (sEVs; Fig. 1B-E, Fig. S1F-G, Fig. S2A-B). When we compared afEV formation induced by stimulation of PMNs with wt and *pksP* mutant conidia, which lack the pigment and virulence determinant dihydroxynaphthalene melanin (25, 40-43), we discovered that melanin-deficient conidia doubled the production of EVs (Fig. 1C-E). This finding suggests that fewer EVs are produced against melanized wt conidia, consistent with a known repressive role for dihydroxynaphthalene melanin against the host immune response during infection (44). For clarity, we have defined EVs induced by wt conidia as antifungal EVs (afEVs), EVs induced by *pksP* mutant conidia as *pksP* EVs, and spontaneously produced EVs as sEVs. Despite this major difference in EV production, PMN viability was similar for wt and *pksP* mutant conidia-infected cells (Fig. S2C); however, *pksP* conidia did exhibit higher opsonization (Fig. S2D; (42)). The vesicular nature of the detected EVs was verified by detergent treatment using 1% (v/v)-Triton X-100, which led to the disappearance of signals for both Annexin V and EV surface marker staining (Fig. S1F and S1G). Cryo-transmission electron microscopy (TEM) imaging (Fig. 1F-M) confirmed a heterogeneous population of circular structures with lipid bilayers for both afEVs and sEVs (26, 45). Both types of EVs appeared to contain

cargo with different spatial organization (Fig. 1G-I and K-M), including practically empty EVs (Fig. 1G and 1K), granular structures (Fig. 1H and 1L), and homogenous distribution of cargo (Fig. 1I and 1M).

afEVs are enriched for antimicrobial proteins

We next addressed the cargo of EVs in response to infection. We purified proteins from afEVs, *pksP* EVs, and sEVs. Equal amounts of protein were labelled with tandem mass tags (TMT) or left unlabeled for a subsequent label-free quantification (LFQ), followed by detection with nano-scale liquid chromatographic tandem mass spectrometry (nLC/MS-MS; Dataset S1 and Dataset S2). LFQ analysis revealed an expanded proteome in the afEVs and *pksP* EVs compared to the sEVs, and suggestive of additional functionality (Fig. 2A). We next compared i) *pksP* EVs *vs.* afEVs, ii) afEVs *vs*. sEVs, and iii) *pksP* EVs *vs.* sEVs. We observed that the afEVs and *pksP* EVs were again quite different from the sEVs, but even afEVs differed from *pksP* EVs (Fig. 2B-D). Analysis using the TMT method of quantification also indicated differences in each population, consistent with the LFQ data (Fig. S3A-C). Since EVs are often enriched for membrane proteins, we next predicted transmembrane domain-containing proteins using three different tools (TMHMM (46), SignalP (47), and WoLF PSORT (48)) and identified 17 proteins in the TMT dataset and 29 proteins in the LFQ dataset (Table S1).

In comparison to sEVs, both afEVs and *pksP* EVs contained a broader spectrum of proteins, and more importantly, higher amounts of antimicrobial peptides such as histones H2A, H2B, and H3.1, neutrophil elastase (NE), myeloperoxidase (MPO), cathepsin G, azurocidin, and defensin 1 (Table 1). CD11b and CD63 were enriched in afEVs and *pksP* EVs compared to sEVs, thus confirming the flow cytometry data (Table 1, Fig. 1D and 1E). In addition, afEVs contained higher

amounts of metabolic enzymes such as glucose-6-phosphate isomerase and transketolase, the cell surface glycoprotein CD177, and F-actin. Proteins of the antimicrobial calprotectin complex (S100-A8, S100-A9) exhibited the highest absolute abundance in afEVs (Tables S2 and S3). Finally, afEVs and *pksP* EVs were more similar in protein content in comparison to sEVs (Table 1).

Table1. Examples of differentially-produced proteins.

UniProt Accession	**Protein**	**TMT ratio** *pksP* EVs/ afEVs	**TMT ratio** afEVs/sEVs	**TMT ratio** *pksP* EVs/sEVs
A0A0U1RRH7	Histone H2A	1.32	14.08	18.55
U3KQK0	Histone H2B	1.12	6.27	7.04
P68431	Histone H3.1	0.82	16.84	13.79
P08246	Neutrophil elastase	0.62	4.64	2.86
P05164	Myeloperoxidase	1.19	2.16	2.57
P08311	Cathepsin G	0.73	3.07	2.24
P20160	Azurocidin	0.70	3.46	2.41
P59665	Defensin 1	2.04	13.41	27.37
P11215	CD11b (Integrin alpha M)	0.85	3.49	2.95
P08962	CD63	1.06	4.99	5.31
A0A087WVM2	CD177	0.88	2.72	2.40

The comparison of the proteins from all EV subsets revealed that 60 proteins were shared between all groups, suggesting that these proteins are part of the core EV protein set. Gene ontology (GO)-term enrichment analysis of the 60 shared proteins revealed overrepresentation of proteins involved in Fc-γ receptor signaling, Arp2/3 complex-mediated actin nucleation, the IL-8 signaling pathway, cytoskeletal rearrangements, and positive regulation of actin polymerization (Fig. 2, Fig. S3D). In comparison to the literature, we found 164 proteins in common between Timar *et al*. (34) and this study. We detected 118 proteins unique to the Timar *et al*. study, and 448 proteins unique to our study using LFQ-based proteomics. Infection with wt or *pksP* conidia led to formation of afEVs and *pksP* EVs with distinct proteome cargos,

characterized by increased levels of antimicrobial peptides and metabolic proteins. These findings suggested an antimicrobial function for afEVs.

afEVs influence fungal growth by inhibition of hyphal extension

To prove a potential antifungal activity of afEVs, we collected afEVs and *pksP* EVs from PMNs, coincubated them in different concentrations with resting conidia, and monitored fungal growth by confocal laser scanning microscopy (CLSM; Fig. 3A and Fig. S4A-B). The area of objects (single hyphae or clusters) was considered as the growth measure. The concentration of EVs was measured in “doses”. One dose of EVs was defined as the number of *pksP* EVs produced by 10^7 PMNs infected with *pksP* mutant conidia at 2 h post infection. At this time point, we found a relatively large amount of produced EVs (Fig. 1C) associated with a relatively low fraction of apoptotic bodies (Fig. 1B). Doses for each condition were normalized according to abundance, from observations in Fig. 1C. The afEVs generated by PMNs infected with wt conidia strongly inhibited the growth of wt and *pksP* hyphae in all donors when 3× doses of EVs were applied (Fig. 3B-E and Fig. S4C-F). These experiments revealed donor-heterogeneity in response to four different donors. 3× doses of *pksP* EVs, as well as single doses of afEVs, were efficient in growth arrest of hyphal filaments in one donor only (Fig. 3D, Fig. S4E). The fungistatic effects of afEVs for all donors were not due to delayed germination of conidia but rather resulted from the inhibition of hyphal extension (Fig. 3A and 3F, Fig. S4A, S4B, and S4G). Interestingly, sEVs had no impact on the growth of fungi (Fig. 3G). Thus, PMNs produce tailored afEVs with distinct functional properties in response to co-incubation with *A. fumigatus*.

afEVs associate with fungal cells

As discussed above, we observed that afEVs are capable of arresting fungal growth. To study the interactions of afEVs with fungi, we collected three-dimensional (3D) confocal fluorescent image stacks of wt hyphae coincubated with afEVs and *pskP* hyphae coincubated with *pksP* EVs after 20 h of incubation. We quantified the interactions of EVs and hyphae using 3D image analysis to evaluate the densities of EVs within calcofluor white staining (inside) of hyphae (EV volume inside hyphae normalized to hyphae volume) compared to the corresponding EV densities outside hyphae cell wall staining. Densities of EVs inside hyphae (indicating association or internalization of EVs) were significantly higher than EV densities outside hyphae (unassociated with hyphae) for both wt and *pksP* hyphal filaments (Fig. 4A, Movies S1 and S2). The 3D image analysis of fluorescence signals revealed extensive binding of EVs induced by conidia of both fungal strains to hyphae, despite interrogation of equal volumes of EVs and hyphae (Fig. S5A and S5B).

We further assessed the ability of afEVs to associate with hyphae by evaluating the volume of hyphae-associated EVs, which were defined as the sum of the volumes of afEVs bound to the cell wall or internalized into hyphae (Movies S1 and S2). The ability of afEVs to associate with hyphae was mainly dependent on the intrinsic properties of the donors' afEVs (Fig. S5C), while the relative volume density of afEVs had a much smaller effect (Fig. S5D-S5E). We next defined hyphae-associated DNA staining as PI^+ signals colocalized with hyphae, which is indicative of hyphal cell damage. The amount of hyphae-associated DNA staining from hyphae incubated with afEVs was significantly higher than the amount of hyphae-associated DNA staining from control hyphae grown alone, as quantified by the hyphae-associated DNA staining positive volume normalized over the hyphae volume (Fig. 4B and Movie S2). The 3D image analysis also showed that PI^+ staining of hyphae was associated with the interaction of hyphae-associated EVs. In fact, more than

60% of the volume of PI^+ hyphae were associated with hyphae-associated EVs (Fig. S5E and Movie S2). All donor EVs were capable of eliciting PI staining of hyphae, but the extent of this effect was donor dependent (Fig. S5E). Our data imply that afEVs are fungistatic and appear to cause cell damage in a process likely associated with the physical interaction of hyphae and afEVs. In support of this finding, hyphae appear to undergo hyperbranching away from the afEV layer in response to treatment (Movie S3), again suggesting antifungal activity.

The effect of afEVs on fungi led us to test for physical long-term alterations of cell wall morphology. To visualize these changes we obtained scanning electron microscopy (SEM) images of wt hyphae 50 h post afEV treatment. Treated hyphal filaments (Fig. 4C) were again shorter, further confirming the antifungal nature of afEVs. Additional imaging showed slight alterations in the porousness of the cell surface, which included ruffling and invaginations that were not observed in hyphae grown without afEVs (Fig. S6). Next, we took advantage of a previously reported mitochondrial GFP cell death reporter strain (AfS35 pJW103) produced to monitor granulocyte killing of *A. fumigatus* (49). In this strain, a mitochondrial-localized GFP indicates filamentous, healthy mitochondria in living fungi, but becomes fragmented upon initiation of cell death pathways, and ultimately loses fluorescence at later time points. Using this strain, we were able to observe mitochondrial fragmentation and limited growth of 20-h-old hyphae challenged with afEVs or an H_2O_2 control (3 mM), but not *pksP* EVs or sEVs (Fig. 5). These results indicate a fungicidal activity for afEVs and are consistent with the results from Fig. 3.

To further support our findings of afEVs in association with fungal cells, we performed 3D image analysis of afEV entry into GFP-expressing hyphae. The obtained data demonstrated that afEVs could be incorporated into the fungal cytoplasm (Fig. 6A-D, Movie S2). Furthermore, we were able to differentiate four

locations of EV-fungal interactions: i) the largest fraction of afEVs, 50-70% (referred to as type I afEVs), were cell-wall associated EVs; ii) afEVs embedded into the cell wall amounted to 0.5-2.5% of EVs; iii) 15-45% of afEVs were found to be located at the interface between cell wall and cytoplasm; and iv) intracytoplasmic afEVs represented 0.2-3% of all afEVs (Fig. 6A-D, Movie S2).

afEV proteins are toxic to fungal cells

We next assessed whether the antimicrobial proteins found in afEVs might contribute to growth inhibition of hyphae when expressed heterologously in the fungus. The genes of two of these human proteins, cathepsin G and azurocidin, were selected because both proteins were enriched in afEVs and were also known to have antifungal effects. For example, cathepsin G knockout mice are highly susceptible for an *A. fumigatus* infection (50, 51). The encoding genes were placed under inducible expression in *A. fumigatus* hyphae (Fig. S7A-B). As a control, we also placed the human retinol binding protein 7 (RBP7), a protein detected in EVs with no expected antifungal activity under inducible expression in *A. fumigatus* hyphae as well (AfRBP7). Addition of the inducer, doxycycline, to cultures of the transgenic *A. fumigatus* strains (AfcathG and Afazuro) led to a massive growth reduction, further demonstrating that the cargo of afEVs can limit fungal growth when active in the fungus, whereas the control RBP7 strain (AfRBP7) revealed no change in dry weight (Fig. 7A and 7B). The presence of the human proteins in hyphae after induction with doxycycline was confirmed by LC-MS measurements of fungal protein extracts (Fig. 7C).

Discussion

Neutrophils are critical for elimination of *A. fumigatus* from the human host (52); however, the exact extracellular mechanisms of how PMNs kill *A. fumigatus* hyphae are not known (52). *A. fumigatus*-triggered neutrophil extracellular traps are slightly fungistatic but do not account for the full activity of neutrophils (22, 23). Here, we show that *ex vivo* applied human EVs triggered by wt conidia (afEVs) inhibit the growth of hyphae and elicit cell damage, adding a new mode of antifungal defense against *A. fumigatus*. These results are consistent with previous findings from PMN-derived EVs showing antibacterial effects against *Staphylococcus aureus* (34). We speculate that afEVs are produced primarily as a result of fungal-driven PMN activation, as apoptotic bodies accounted for less than 10% of the total EV population.

afEV production was increased in response to *A. fumigatus* infection, as confirmed by flow cytometry. EVs increased with kinetics different from those previously reported for anti-*S. aureus* PMN-derived EVs, where maximum production was observed at 20 min (34). The interaction of PMNs with *A. fumigatus* conidia resulted in an enrichment of CD63 on afEVs, which was not observed in antibacterial EVs (34) and is typically only found on EVs smaller than 100 nm. afEVs were also enriched in MPO, NE, and cathepsin G, consistent with their antifungal function. Interestingly, and further supporting the importance of afEV cargo is the finding that cathepsin G, NE, and calprotectin knockout mice are all highly susceptible to infection with *A. fumigatus* (11, 50). It is possible that these proteins serve an EV-independent role in host defense; however, many of these proteins have been shown to be associated with EVs in our study and previous studies (26, 34).

Our proteomic analysis of EVs indicated that afEVs and *pksP* EVs contained an expanded proteome compared to sEVs; however, nearly all proteins from afEVs were found in *pksP* EVs. Despite this overlap, the abundance of these cargo proteins

was quite different. These results are consistent with a hypothesis that the abundance of EV cargo proteins dictates the antifungal nature of that EV population. Our results also suggest that the cargo of afEVs is tailored to the pathogen, as wt and *pksP* conidia elicited different responses. It is important to note that the *pksP* mutant utilized in these studies is not a knockout, but instead derived from a UV-mutagenized strain (53). Previous work has indicated that the phenotypes observed with this strain are due to the inactivation of *pksP* and that they could be fully complemented by the wt *pksP* gene (42, 53). Our findings also suggest a novel function for the fungal virulence factor dihydroxynaphthalene-melanin (54, 55) in modulating EV biogenesis and protein cargo. Melanized conidia are less opsonized than non-melanized conidia, and as a consequence, show reduced phagocytosis by neutrophils, which might lead to lower afEV production (42). This hypothesis is also supported by the observation that CD11b and CD63 receptors are differentially expressed on the surface of neutrophils during confrontation with *pksP* and wt conidia.

Our results demonstrate that afEVs associate with fungal hyphae, as evidenced by the high proportion of EVs colocalized with the cell wall of the fungus. In addition, since EVs were found intracellularly, inhibition and killing of the fungus might be due to a combination of these adherence and penetration mechanisms. Human primary neutrophils cannot be genetically manipulated to knock out azurocidin or cathepsin G, so we instead created *A. fumigatus* strains that produce cathepsin G and azurocidin using an inducible promoter system. The production of these proteins in the fungus clearly led to a massive growth defect, suggesting that delivery of these cargos could contribute to antifungal activity; however, this experiment offers only a proof-of-principle. In addition, we observed that fungal hyphae move away from afEVs by hyperbranching, suggesting that the fungus

actively avoids afEVs. This finding is consistent with other observations of hyperbranching away from neutrophils during infection (56).

Our 3D image analysis and work with a mitochondrial GFP reporter strain revealed the potential of afEVs to induce fungal cell damage, while also revealing afEV association with hyphae and a fungicidal capacity. Interestingly, PMN-generated reactive oxygen species (ROS) were recently shown to induce fungal cell death (14), and perhaps there is a connection between ROS-induced fungal cell death and afEV toxicity. More work will be required to fully elucidate the mechanism of fungal killing by afEVs. Our data did show that the intracellular production of antimicrobial peptides could contribute to a severe inhibition of fungal growth. On the other hand, neutrophil EV-associated effector functions are also known to contribute to innate immune pathology. For example, the surface-bound neutrophil elastase of EVs has been shown to cause extracellular matrix destruction and disease in the lungs of COPD patients and could help explain the antifungal activity of afEVs (57).

In conclusion, our results suggest that human PMNs release afEVs in response to an *A. fumigatus* infection. These EVs contain a cargo of antimicrobial proteins that inhibit hyphal growth and kill hyphae. We envision that the analysis of EVs produced in bronchoalveolar lavage-fluid represents a potentially useful tool for diagnostic and/or prognostic markers of IA. Although we hypothesize that afEVs serve as an important factor in the control of pathogenesis during *A. fumigatus* infection, much work remains to completely unveil the function of these important intercellular mediators.

Methods

Ethics statement

This study was approved by the Institutional Review Board of the Jena University Hospital (approval number: 2395-10/08 and 5074-02/17) in agreement with the Declaration of Helsinki. Informed consent has been obtained for study participation. PMNs were isolated from fresh venous blood of healthy adult volunteers collected after obtaining written consent.

Strains, growth conditions, and fungal biomass determination

A. fumigatus ATCC 46645, the GFP-expressing strain AfS148 (58), the melanin-free *pksP* mutant (53), and the mitochondrial GFP reporter strain AfS35 pJW103 (49) were maintained on malt extract (Sigma-Aldrich) agar plates supplemented with 2% (w/v) agar for 5 days at 37ºC. When appropriate, *A. fumigatus* ATCC 46645 and the overexpression strains *A. fumigatus* Afazuro, AfcathG, and AfRBP7 were cultivated on *Aspergillus* Minimal Medium (AMM) for 3 days at 37°C, as described (59). All conidia were harvested in sterile deionized water, filtered through 40 µm cell strainers (BD Biosciences, Heidelberg, Germany), washed, and resuspended in deionized sterile water. Spore suspensions were counted in a Thoma chamber and stored at 4°C for no longer than 1 week. Freshly harvested spore suspensions were used for each experiment.

For biomass determination, 10^8 conidia/ml were inoculated in 100 ml AMM, supplemented with 10 µg/ml doxycycline when needed for induction of tet^{ON} promoter, and grown at 37°C at 200 rpm for 24 h. Mycelia were collected, washed, filtered through Miracloth, and dried at 60°C for 3 days before weighing.

Opsonization of fungi

Fresh venous blood from adult male healthy volunteers, aged 20-35 years, was withdrawn after informed written consent and used for preparation of normal human

serum (NHS). Volunteers had not taken any anti-inflammatory medications for >10 days and had not consumed alcohol for >3 days prior to donation. NHS was obtained by pooling serum prepared from fresh venous blood of seven healthy human donors. Serum was stored at -80°C until use. Conidia were opsonized in 50% (v/v) NHS and 50% (v/v) Hank's balanced salt solution (HBSS) (HyClone, GE Healthcare) for 1 h at 37°C at 500 rpm in duplicate. Conidia were pelleted by centrifugation at 16,000 × *g* at 4°C for 10 min and subsequently washed three times with HBSS prior to confrontation assays with PMNs.

To measure C3 deposition on the conidial surface after opsonization, conidia were washed three times with Dulbecco's phosphate buffered saline (DPBS) and then incubated with a 1:1000 dilution of polyclonal goat anti-human C3 serum (Comptech) in 3% (w/v) BSA for 1 h at RT. This was followed by addition of a 1:400 dilution of Alexa Fluor 647-conjugated donkey anti-goat IgG (Invitrogen) secondary antibody in 3% (w/v) BSA for 1 h at RT. Fluorescence of 10,000 conidial cells was measured by flow cytometry (BD LSR II), and the median fluorescence intensity of each conidial population was calculated using FlowJo software (Becton Dickinson, USA).

PMN isolation

PMNs were isolated from fresh venous blood of healthy adult volunteers with purity above 95% and viability at 98% as described in detail (26) with slight modifications as follows: blood was collected in K_2EDTA BD Vacutainer tubes (BD Biosciences) and Biocoll Separation Solution (Biochrom, GE Healthcare) or PolymorphPrep (PROGEN) was used for gradient centrifugation. Neutrophil purity was determined using an antibody cocktail as follows: CD3-PE (clone SK7; dilution 1:50), CD14-V500 (M5E2; 1:200), CD16-APC-Cy7 (3G8; 1:50), CD19-AF700 (cloneHIB19; 1:100),

CD56-FITC (NCAM16.2; 1:100), and CD66b-PerCP-Cy5.5 (G10F5; 1:66) obtained from BD Pharmingen and CCR3-APC (5E8; 1:40) from Biolegend. Cells (1×10^6) were blocked with 5% (v/v) mouse serum and then stained for CCR3 for 10 min at 37ºC. Subsequently, an antibody cocktail mix was applied for staining of the remaining antigens from the above mentioned panel for an additional 30 min at RT. For cell damage assays at each time point, 2×10^6 neutrophils in 200 µl of HBSS were incubated with PI (5 µg) and Alexa 647-annexin V (5 µl) for 15 min at RT. Then, the cells were centrifuged at 400 × *g* for 5 min and resuspended in 500 µl DPBS. Fluorescence of 10^4 gated neutrophils was measured by flow cytometry with a BD LSR II (BD Biosciences) using BD FACSDiva Software Version 8.0.1 (BD Bioscience). Data were analyzed with FlowJo software.

EV isolation and characterization

EVs were prepared following a procedure by Timar *et al.* (34) with slight modifications. PMNs with a density of $1x10^7$ cell/ml were confronted with opsonized wt *A. fumigatus* ATCC 46645 or opsonized *A. fumigatus pksP* mutant conidia with an MOI of 10 or 5 in HBSS with Ca^{2+} and Mg^{2+} (HyClone, GE Healthcare) on a linear shaker (100 rpm) at 37°C for 4 h. EVs produced by uninfected PMNs (sEVs) served as negative control. At the selected incubation time points, PMNs were sedimented for 10 min with 1000 × *g* at 4°C on 45° fixed-angle rotor FA-45-30-11 (Eppendorf). The supernatant was filtered by gravity through sterile PVDF 5.0 µm Millex syringe filters (Merck-Millipore). EV suspensions were stained with a cocktail of fluorescence-conjugated mAbs (PerCP/Cy5.5-anti-human-CD63, clone H5C6 from Biolegend; RPE-CD11b from Dako; and FITC-Annexin V from Biolegend) for 20 min at RT and centrifuged on 45° fixed angle rotor FA-45-30-11 (Eppendorf) for 20 min, 4°C, 19,500 × *g*. Corresponding single-stained Ab isotype controls were also prepared

(PerCP/Cy5.5 mouse IgG1, κ isotype (MOPC-21) from Biolegend; mouse IgG1, κ isotype RPE-CD11b from Dako). After centrifugation the supernatant was carefully aspirated and EV pellets were resuspended in the original incubation volume in HBSS.

The size distribution of PMN-derived EVs was recorded with a Nanotrac Flex 180° dynamic light scattering system (Microtrack) at 22°C. At least 20 measurements per sample were performed and the average hydrodynamic radius was calculated with the sphere approximation using the FLEX11 software.

Flow cytometry measurements of EVs were conducted on BD LSR Fortessa using the BD FACs Diva Software Version 8.0.1 (BD Biosciences) applying an optimized EV flow protocol (60). Briefly, pure HBSS was used to record instrument noise. The upper size limit detection threshold was set by fluorescent rainbow particles with mid-range intensity and size 3.0-3.4 µm (Biolegend) resuspended in HBSS. Stained EV suspensions were enumerated in the fluorescent gate above the gate of the negative isotype-labelled controls. Once measured, samples were treated with 1% (v/v) Triton X-100 to verify the vesicular nature of the detected events. Detergent-resistant events (false positives) were subtracted from the total measured events using the FlowJo version 10.0.7 from Tree Star software.

Electron Microscopy (Cryo-TEM and SEM)

For ultrastructural investigations isolated EVs were imaged with cryo transmission electron microscopy (cryo-TEM) and EV effects on fungi were studied with scanning electron microscopy (SEM).

For cryo-TEM imaging sEVs and afEVs collected at a time point of 2 h were freshly prepared using neutrophils from the same male donor and immediately subjected to imaging. 5 µl of purified pelleted EVs in HBSS were applied to carbon-

coated copper grids (R1.2/1.3, Quantifoil Micro Tools GmbH) and the excess of liquid was blotted automatically for two seconds from the reverse side of the grid with a strip of filter paper. Subsequently, the samples were rapidly plunged into liquid ethane (cooled to -180°C) in a cryobox (Carl Zeiss NTS GmbH). Excess ethane was removed with a piece of filter paper. The samples were transferred with a cryo-transfer unit (Gatan 626-DH) into the pre-cooled cryo-TEM (Philips CM 120) operated at 120 kV and viewed under low dose conditions. The images were recorded with a 2k CMOS Camera (F216, TVIPS, Gauting).

SEM analysis was used to investigate the effect of afEVs on the growth of *A. fumigatus*. Therefore, wt conidia were coincubated with 3× dose of PMN-derived EVs for 50 h in HBSS at 37ºC in the dark. At the end of the coincubation time, samples were fixed in 2.5% (v/v) glutaraldehyde in HBSS on Isopore™ membrane TMTP filters with pore size 5 µm (Merck-Millipore) for 30 min followed by washing thrice with HBSS buffer (10 min each). Then, the samples were dehydrated in ascending ethanol concentrations (30, 50, 70, 90, and 96% (v/v)) for 10 min each by thoroughly rinsing the membranes and soaking through the liquids with blotting paper. Subsequently, ethanol was changed with hexamethyldisilazane (Merck) in two steps (50%, 96% (v/v)), and samples were air-dried. Afterwards, the samples were sputter-coated with gold (thickness approx. 4 nm) using a SCD005 sputter coater (BAL-TEC, Liechtenstein) to avoid surface charging and investigated with a field emission (FE) SEM LEO-1530 Gemini (Carl Zeiss NTS GmbH).

LC-MS/MS-based proteome analysis of EVs

For proteome analysis of EVs, purified sEVs, afEVs, and *pksP* EVs were collected from a pool of 20 different donors in HBSS and stored at -80°C for no longer than 1 week prior to protein extraction. EV suspensions were concentrated on 3 kDa

483 polyethersulfone (PES) membrane centrifugal filters (VWR International) for 5 min at
484 14,000 rpm at 4°C (Sigma 3-KIS centrifuge). Samples were snap-frozen in liquid N_2
485 and delipidated by protein precipitation based on the protocol of Wessel and Flügge
486 (61). Proteins were resolubilized in 50 µl 50 mM triethyl ammonium bicarbonate
487 (TEAB) in 1:1 trifluoroethanol (TFE)/H_2O and denatured for 10 min at 90°C. Protein
488 quantification was performed using the Direct Detect® system (Merck-Millipore). Each
489 sample was set to 40 µg of total protein in 100 µl in 100 mM TEAB. Proteins were
490 reduced with 10 mM tris(2-carboxyethyl) phosphine (TCEP) at 55°C for 60 min and
491 alkylated with 12.5 mM iodoacetamide (IAA) at RT for 30 min in the dark. Proteins
492 were digested for 2 h at 37°C with Lys-C and 16 h at 37°C with Trypsin Gold (both
493 Promega). For TMT 6-plex labeling (Thermo Fisher Scientific), digested peptides
494 were treated according to the manufacturer's instructions. Labelled peptides were
495 pooled and fractionated offline on HyperSep SCX (strong cation exchange) columns
496 (Thermo Fisher Scientific).

497 LC-MS/MS analyses and protein database searches were performed as
498 described in Baldin et al. (62) with the following modifications: gradient elution of A
499 (0.1% (v/v) formic acid in water) and B (0.1% (v/v) formic acid in 90/10
500 acetonitrile/water (v/v)) was as follows: 0-4 min at 4% B, 15 min at 5.5% B, 30 min at
501 7% B, 220 min at 12.5% B, 300 min at 17% B, 400 min at 26% B, 450 min at 35% B,
502 475 min at 42% B, 490 min at 51% B, 500 min at 60% B, 515-529 min at 96% B, 530-
503 600 min at 4% B. Precursor ions were measured in full scan mode within a mass
504 range of m/z 300-1500 at a resolution of 140k FWHM using a maximum injection time
505 of 120 ms and an AGC (automatic gain control) target of 3×10^6 (TMT) or 1×10^6
506 (LFQ). The isolation width was set to m/z 0.8 (TMT) or 2.0 (LFQ) amu. Tandem mass
507 spectra were searched by Proteome Discoverer (PD) 2.1 (Thermo Fisher Scientific
508 Waltham) against the UniProt database of *Homo sapiens* (22/08/2016) using the

algorithms of Mascot v2.4.1 (Matrix Science), Sequest HT and MS Amanda (63). Dynamic modifications were oxidation of Met (LFQ) and TMT-6-plex reaction at Tyr (not considered for quantification). Static modifications were carbamidomethylation of Cys by iodoacetamide (LFQ) and TMT-6-plex reaction at Lys and the peptide N-terminus. The TMT significance threshold for differentially abundant proteins was set to factor ≥1.5 (up- or down-regulation). The data was further manually evaluated based on the average reporter ion count (≥2 for medium confidence, ≥4 for high confidence). Furthermore, the average variability was observed as a function of the differential regulation and the reporter ion count. Label-free quantification was performed by the Precursor Ions Area method of PD 2.1. The mass tolerance was set to 2 ppm and the signal-to-noise ratio had to be above 3. The abundance values were normalized based on the total peptide amount. The significance threshold for differential protein abundance was set to factor ≥2.0 (up- or down-regulation). The mass spectrometry proteomics data have been deposited to the ProteomeXchange Consortium *via* the PRIDE partner repository with the dataset identifier PXD005994 (64).

Functional annotation of the EV proteome

The dataset of differentially regulated proteins was filtered by the human serum proteome represented in Piper and Katzmann (65) and in addition, by keratin, epidermal proteins and complement component 5α, which were not considered for the proteome comparison. The filtering and the overlap analyses were performed in R using packages provided by Bioconductor (66). The GO-term enrichment analysis of the overlapping proteins of the TMT datasets was performed using FungiFun2 (67). The results contain categories determined by Fisher's exact test and Benjamini-Hochberg corrected p-values below 0.05.

Analysis of heterologously expressed human azurocidin and cathepsin G

Protein preparation and LC-MS/MS analysis and database search for identification of proteins was essentially performed as previously described (62) except the following changes: LC gradient elution was as follows: 0 min at 4% B, 5 min at 5% B, 30 min at 8% B, 60 min at 12% B, 100 min at 20% B, 120 min at 25% B, 140 min at 35% B, 150 min at 45% B, 160 min at 60 %B, 170-175 min at 96% B, 175.1-200 min at 4% B. Mass spectrometry analysis was performed on a QExactive HF instrument (Thermo) at a resolution of 120,000 FWHM for MS1 scans and 15,000 FWHM for MS2 scans. Tandem mass spectra were searched against the UniProt database (2018/07/08, https://www.uniprot.org/proteomes/UP000002530) of *Neosartorya fumigata* (Af293) and the human protein sequences of azurocidin, cathepsin G, and RBP7, using Proteome Discoverer (PD) 2.2 (Thermo) and the algorithms of Sequest HT (version of PD2.2) and MS Amanda 2.0. Modifications were defined as dynamic Met oxidation and protein N-term acetylation as well as static Cys carbamidomethylation.

Determination of EV effects on fungi by CLSM

For determining EV effects on fungi, EVs were dosed according to cell equivalents. One EV dose was defined as the number of EVs produced by 10^7 PMNs infected with *pksP* mutant conidia at an MOI of 5 at 2 h post infection, which represented the maximal observed production of EVs (Fig. 1C) and corresponded to approximately 10^9/ml EVs by nanoparticle tracking analysis with a Malvern NS300 (camera setting, 14; detection threshold, 4). At this time point, *pksP* conidia stimulated double the EVs as wt conidia and 12-fold more than sEVs from the same number of cells. Consequently, doses were adjusted to appropriately compare equal numbers of EVs. Freshly prepared and portioned EVs were coincubated with 30 µl of a suspension of

10^6 conidia/ml in HBSS in 12-well chambers (Ibidi GmbH). A confocal laser scanning microscopy (CLSM) system, Zeiss LSM 780 (Carl Zeiss SAS), was employed; see section “CLSM Setup” for details. Images were acquired once per hour from ten different fields of view per well in a microtiter plate. The 2D confocal images were recorded at 208 by 208 nm pixel size, whereas 3D image stacks had a voxel volume of 0.025 (19 samples) or 0.034 (15 samples) μm^3.

After 20 h, the samples were stained with Annexin-V FITC (1:60; Biolegend), PI (to a final concentration of 0.0167µg/µl) and calcofluor white (to a final concentration of 0.167 µg/µl) in order to assess EV entry into hyphae and to collect image Z-stacks by CLSM. When the *A. fumigatus*-GFP strain AfS148 was used, the staining cocktail consisted of Annexin V-Alexa 647 and calcofluor white, whereas PI staining was omitted in order to avoid spectral overlaps.

For investigation of EV-mediated fungal killing, we took advantage of a previously described mitochondrial GFP-expressing reporter strain AfS35 pJW103 (49). When growing normally, this fungal strain shows a normal filamentous network of mitochondria indicated by mitochondria-specific fluorescence. For these experiments, 10^6 conidia/ml of strain AfS35 pJW103 were grown in HBSS in 8-well chambers (Ibidi GmbH) for 20 h prior to coincubation with freshly prepared EV fractions. Here, we used EVs collected from equal amounts of PMNs (10^7 PMNs). A CLSM system, Zeiss LSM 780 (Carl Zeiss SAS), was used to monitor mitochondrial fragmentation (GFP signal) and cell growth (calcofluor white) over time. As a control, cell death was initiated using 3 mM H_2O_2, which causes the mitochondria to undergo fusion and form punctate structures within one hour and then fade in fluorescence signal over time (49).

CLSM setup

The imaging data were collected with a Zeiss LSM 780 confocal laser scanning microscope (Carl Zeiss SAS). Images were taken using either a 10x/NA 0.4 or a 20x/NA 0.7 objective lens in inverted configuration, resulting in a total magnification of 100x or 200x, respectively. In order to measure the point-spread function of the CLSM system, 5 µl of the blue, green, and deep-red calibration beads from the PS-Speck Microscope Point Source Kit (diameter 170 nm; Invitrogen) were resuspended in the staining cocktail. The bead mixture was imaged under the same conditions as applied for the Z stacks of the hyphae-EV system. Individual 3D bead images were averaged per-color by HuygensPro and the resulting 3D bead images were used to distill the measured point-spread function for all three colors. For imaging hyphae and EVs, the CLSM objective lens and stage were preheated to 37ºC for 3-5 h prior to image scanning. Bright field images were acquired from 10 different fields of view per well, once per hour for 15 time points using a 20x/NA 0.8 dry objective at 37ºC, in 5% (v/v) CO_2 atmosphere.

For the Z-stacks, images were collected at an axial separation that was set according to the Nyquist criterion for the shortest wavelength, using the same Z step size for all channels. The axial range was adjusted to the thickness of the observed cells.

3D image analysis of EV internalization

For a quantitative analysis of the afEVs-hyphae interactions, the 3D shape of each object type was reconstructed based on 4D (3D plus color) fluorescence images using the following procedure: the images were deconvolved using HuygensPro (SVI, Hilversum, The Netherlands) with a measured PSF (see section “CLSM Setup”) that was recorded individually for each fluorescence channel. The deconvolved images were transferred to Imaris (Bitplane, Zürich, Switzerland) for 3D reconstruction. The

basic object types (hyphae, DNA, EVs) were reconstructed in Imaris using manually adjusted templates. The reconstructed hyphae only included objects from the calcofluor white channel (see Determination of EV effects on fungi by CLSM) that were larger than 20 μm^3 and had no surface points on the sample border. The reconstruction process is presented in Movies S1-3. The control samples and those with GFP fluorescence were reconstructed using the same procedure. Hyphae-associated DNA and hyphae-associated EVs were identified by using a binary mask of the hyphae (channel 4; Movie S2). Only those objects were assigned as hyphae-associated that were located either on the border or inside the hyphae, as identified by a threshold of the mean value of the calcofluor white fluorescence signal being above 5×10^{-10}. The binary mask of hyphae-associated EVs was used to select hyphae-associated DNA that interacted with EVs (hyphae-associated DNA, mean value of binary mask of hyphae, Movie S2). Finally, the total volume of each object class at every field of view was computed. Additionally, the EV volume inside hyphae was computed over the regions that were double-positive for Annexin V (EVs) and calcofluor white (hyphae), whereas the EV volume outside hyphae was defined as the volume that was positive for Annexin V but not in calcofluor white. EV densities inside and outside hyphae were then defined as follows:

$$\text{EV density inside} = \frac{\text{EV volume inside hyphae}}{\text{Hyphae volume}}$$

$$\text{EV density outside} = \frac{\text{EV volume outside hyphae}}{\text{Sample volume-Hyphae volume}}$$

The sample volume was estimated based on voxel size and number of voxels in each sample (automatically performed by Imaris).

Automated 2D image analysis of hyphal growth

For quantitative analysis of hyphal growth in bright field microscopy images, the area of the regions of interest (ROI) corresponding to the conidia and the hyphae, was computed automatically for each image. The image analysis algorithm was implemented in Matlab (Matlab 2017a, MathWorks). The code is available from the authors upon request. The procedure included: (1) binarization of image data, (2) binary image enhancement, (3) selection of ROI based on morphological filtering, (4) image post-processing and filtering, and (5) area measurement of the ROI. Two of the original image sections, together with the resulting images after having applied the aforementioned steps, are illustrated in S4A Fig. All parameters of the algorithm were adjusted to minimize the detection of noise and of out-of-focus objects, which was confirmed by visual inspection of the images. The image data was saved in 16-bit CZI format and loaded into Matlab using the *bfopen* script from the Open Microscopy Environment (https://www.openmicroscopy.org/site/support/bio-formats5.3/developers/matlab-dev.html). The images were processed in five steps:

1. Binarization was performed using the function *imbinarize* from the Matlab ImageProcessing toolbox with the following parameters:

- threshold type: 'Adaptive';
- sensitivity factor for adaptive thresholding: 'Sensitivity'=0.45;
- foreground darker than background: 'ForegroundPolarity'='dark'.

2. Enhancement of the binary image included the following steps:

- *majority filter*: sets a pixel value to 1 if five or more pixels in its 3-by-3 neighborhood have values of 1; otherwise, the pixel value is set to 0;
- hole-filling inside ROI;
- object removal for ROI with area less than 200 pixels, which corresponds to the minimal area of resting conidia.

The resulting image is referred to as image *S*.

3. Selection of ROI:

- splitting of image *S* into two masks, *M* and *S'*, based on the object area: image *M* containing all ROI with an area less than 1000 pixels that correspond to resting, swollen and germinated conidia, as well as parts of vesicle clumps, and image *S'* with all remaining large ROI, corresponding to hyphae;

- removal of all ROI from mask *M* with solidity below 0.85, corresponding to vesicle clumps; the resulting mask is referred to as *M'*;

- combination of masks *M'* and *S'* into one mask *R* by the logical sum operation of *M'* and *S'*.

4. Image post-processing and filtering:

- morphological closing of the mask *R* with two “line”-elements (10 pixels long, orientation 45 and 135 degrees) to connect broken contours;

- removing all ROI that have the 1st percentile of their Feret diameters less than 17 pixels (the size of resting conidia); this removes the remaining vesicle clumps, which have regions thinner than 17 pixels; for the Feret diameters calculation the toolbox “Feret diameter and oriented box” was used (David Legland, https://www.mathworks.com/matlabcentral/fileexchange/30402-feret-diameter-and-oriented-box).

5. Area measurement of the ROI:

- the area of each object was computed using the function *regionprops* with the parameter 'FilledArea';

- the median of the areas of all ROI in an image was used to characterize fungal coverage in the image.

Generation of transgenic *A. fumigatus* strains

For expression of the human azurocidin *AZU1* gene, the human cathepsin G *CTSG* gene and the human retinol binding protein 7 *RBP7* gene in *A. fumigatus*, the tetracycline-controlled transcriptional activation (tet^{ON}) system was used (68). The human azurocidin, cathepsin G and retinol binding protein 7 cDNA sequences obtained from the NCBI database were codon optimized for *A. fumigatus* using the GENEius Tool (https://www.eurofinsgenomics.eu/en/gene-synthesis-molecular-biology/geneius/) and synthesized together with the *tef* terminator (Eurofins Genomics). Each of the genes was PCR-amplified from the corresponding synthetic template using the Phusion Flash High-Fidelity PCR Master Mix (Thermo Fisher Scientific) with the primer pairs Azu_policitail_f and tef_r for azurocidin, cathG_policitail_f and tef_r for cathepsin G and RBP7_policitail_F and tef_r for RBP7 (S4 Table). The tet^{ON} promoter cassette was amplified from plasmid pSK562 with primers ptetOn_pYES2tail_F and pOliC_R, while the pyrithiamine resistance cassette (*ptrA*) was amplified from plasmid pSK275 with primers ptrA_teftail_F and ptrA_pYES2tail_R. Plasmid pYES2 was used as backbone vector and amplified with primers pYES2_r and pYES2_f. The tet^{ON} cassette, each of the three human genes, and the *ptrA* cassette were assembled with the pYES2 backbone using the NEBuilder HiFi DNA Assembly Master Mix (New England Biolabs) according to the manufacturer's instructions. The resulting 10 kb plasmids were sequenced and subsequently used to transform *A. fumigatus* ATCC 46645 as previously described (59). Transformants were selected with 0.1 µg/ml pyrithiamine.

Southern blot analysis to confirm genetic manipulation of *A. fumigatus* strains was carried out as described before (69). For Northern blot analysis, 16-hour-old pre-cultures were treated with 10 µg/ml doxycycline. Mycelia were harvested 3 h post addition of doxycycline. RNA extraction and detection of RNA by Northern blot were carried out as previously described (69).

Data availability

The mass spectrometry proteomics data have been deposited to the ProteomeXchange Consortium *via* the PRIDE partner repository with the dataset identifier PXD005994 (64).

Acknowledgements

We are thankful to all anonymous blood donors, to Ellen Ritter and Tobias Rachow (blood withdrawal), Frank Steiniger (cryo-TEM imaging), and Sven Krappmann (AfS148 strain, pSK562 plasmid). We kindly thank Johannes Wagener for providing the AfS103 pJW103 strain. We thank Silke Steinbach for excellent technical assistance. We thank Maria Straßburger and Thorsten Heinekamp for their contributions to the success of this project.

References

1. Patterson TF, Thompson GR, 3rd, Denning DW, Fishman JA, Hadley S, Herbrecht R, Kontoyiannis DP, Marr KA, Morrison VA, Nguyen MH, Segal BH, Steinbach WJ, Stevens DA, Walsh TJ, Wingard JR, Young JA, Bennett JE. 2016. Practice Guidelines for the Diagnosis and Management of Aspergillosis: 2016 Update by the Infectious Diseases Society of America. Clin Infect Dis 63:e1-e60.

2. Maertens JA, Raad II, Marr KA, Patterson TF, Kontoyiannis DP, Cornely OA, Bow EJ, Rahav G, Neofytos D, Aoun M, Baddley JW, Giladi M, Heinz WJ, Herbrecht R, Hope W, Karthaus M, Lee D-G, Lortholary O, Morrison VA, Oren I, Selleslag D, Shoham S, Thompson GR, III, Lee M, Maher RM, Schmitt-Hoffmann A-H, Zeiher B, Ullmann AJ. 2016. Isavuconazole versus

voriconazole for primary treatment of invasive mould disease caused by *Aspergillus* and other filamentous fungi (SECURE): a phase 3, randomised-controlled, non-inferiority trial. The Lancet 387:760-769.

3. Marr KA, Schlamm HT, Herbrecht R, Rottinghaus ST, Bow EJ, Cornely OA, Heinz WJ, Jagannatha S, Koh LP, Kontoyiannis DP, Lee DG, Nucci M, Pappas PG, Slavin MA, Queiroz-Telles F, Selleslag D, Walsh TJ, Wingard JR, Maertens JA. 2015. Combination antifungal therapy for invasive aspergillosis: a randomized trial. Ann Intern Med 162:81-9.

4. Kosmidis C, Denning DW. 2015. The clinical spectrum of pulmonary aspergillosis. Thorax 70:270-7.

5. Dagenais TR, Keller NP. 2009. Pathogenesis of *Aspergillus fumigatus* in Invasive Aspergillosis. Clin Microbiol Rev 22:447-65.

6. Osherov N, Kontoyiannis DP. 2017. The anti-Aspergillus drug pipeline: Is the glass half full or empty? Med Mycol 55:118-124.

7. Kalleda N, Amich J, Arslan B, Poreddy S, Mattenheimer K, Mokhtari Z, Einsele H, Brock M, Heinze KG, Beilhack A. 2016. Dynamic immune cell recruitment after murine pulmonary *Aspergillus fumigatus* infection under different immunosuppressive regimens. *Front Microbiol* 7:1107.

8. Bonnett CR, Cornish EJ, Harmsen AG, Burritt JB. 2006. Early neutrophil recruitment and aggregation in the murine lung inhibit germination of *Aspergillus fumigatus* conidia. *Infect Immun* 74:6528-39.

9. Mircescu MM, Lipuma L, van Rooijen N, Pamer EG, Hohl TM. 2009. Essential role for neutrophils but not alveolar macrophages at early time points following *Aspergillus fumigatus* infection. J Infect Dis 200:647-56.

10. Dragonetti G, Criscuolo M, Fianchi L, Pagano L. 2017. Invasive aspergillosis in acute myeloid leukemia: Are we making progress in reducing mortality? Med Mycol 55:82-86.

11. Bianchi M, Niemiec MJ, Siler U, Urban CF, Reichenbach J. 2011. Restoration of anti-*Aspergillus* defense by neutrophil extracellular traps in human chronic granulomatous disease after gene therapy is calprotectin-dependent. *Journal of Allergy and Clinical Immunology* 127:1243-1252.e7.

12. Matute JD, Arias AA, Wright NA, Wrobel I, Waterhouse CC, Li XJ, Marchal CC, Stull ND, Lewis DB, Steele M, Kellner JD, Yu W, Meroueh SO, Nauseef WM, Dinauer MC. 2009. A new genetic subgroup of chronic granulomatous disease with autosomal recessive mutations in p40 phox and selective defects in neutrophil NADPH oxidase activity. *Blood* 114:3309-15.

13. Alflen A, Prufer S, Ebner K, Reuter S, Aranda Lopez P, Scharrer I, Banno F, Stassen M, Schild H, Jurk K, Bosmann M, Beckert H, Radsak MP. 2017. ADAMTS-13 regulates neutrophil recruitment in a mouse model of invasive pulmonary aspergillosis. *Sci Rep* 7:7184.

14. Shlezinger N, Irmer H, Dhingra S, Beattie SR, Cramer RA, Braus GH, Sharon A, Hohl TM. 2017. Sterilizing immunity in the lung relies on targeting fungal apoptosis-like programmed cell death. *Science* 357:1037.

15. Espinosa V, Dutta O, McElrath C, Du P, Chang YJ, Cicciarelli B, Pitler A, Whitehead I, Obar JJ, Durbin JE, Kotenko SV, Rivera A. 2017. Type III interferon is a critical regulator of innate antifungal immunity. *Sci Immunol* 2.

16. Bianchi M, Hakkim A, Brinkmann V, Siler U, Seger RA, Zychlinsky A, Reichenbach J. 2009. Restoration of NET formation by gene therapy in CGD controls aspergillosis. Blood 114:2619-22.

17. Boyle KB, Gyori D, Sindrilaru A, Scharffetter-Kochanek K, Taylor PR, Mocsai A, Stephens LR, Hawkins PT. 2011. Class IA phosphoinositide 3-kinase beta and delta regulate neutrophil oxidase activation in response to *Aspergillus fumigatus* hyphae. *J Immunol* 186:2978-89.

18. Boyle KB, Stephens LR, Hawkins PT. 2012. Activation of the neutrophil NADPH oxidase by *Aspergillus fumigatus*. *Ann N Y Acad Sci* 1273:68-73.

19. Levitz SM, Farrell TP. 1990. Human neutrophil degranulation stimulated by *Aspergillus fumigatus*. *Journal of Leukocyte Biology* 47:170-175.

20. Zarember KA, Sugui JA, Chang YC, Kwon-Chung KJ, Gallin JI. 2007. Human polymorphonuclear leukocytes inhibit *Aspergillus fumigatus* conidial growth by lactoferrin-mediated iron depletion. J Immunol 178:6367-73.

21. Braem SG, Rooijakkers SH, van Kessel KP, de Cock H, Wosten HA, van Strijp JA, Haas PJ. 2015. Effective neutrophil phagocytosis of *Aspergillus fumigatu*s is mediated by classical pathway complement activation. *J Innate Immun* 7:364-74.

22. Bruns S, Kniemeyer O, Hasenberg M, Aimanianda V, Nietzsche S, Thywissen A, Jeron A, Latge JP, Brakhage AA, Gunzer M. 2010. Production of

extracellular traps against *Aspergillus fumigatus in vitro* and in infected lung tissue is dependent on invading neutrophils and influenced by hydrophobin RodA. *PLOS Pathogens* 6:e1000873.

23. McCormick A, Heesemann L, Wagener J, Marcos V, Hartl D, Loeffler J, Heesemann J, Ebel F. 2010. NETs formed by human neutrophils inhibit growth of the pathogenic mold *Aspergillus fumigatus*. *Microbes and Infection* 12:928-936.

24. Eken C, Gasser O, Zenhaeusern G, Oehri I, Hess C, Schifferli JA. 2008. Polymorphonuclear neutrophil-derived ectosomes interfere with the maturation of monocyte-derived dendritic cells. *J Immunol* 180:817-24.

25. Eken C, Sadallah S, Martin PJ, Treves S, Schifferli JA. 2013. Ectosomes of polymorphonuclear neutrophils activate multiple signaling pathways in macrophages. *Immunobiology* 218:382-92.

26. Gasser O, Hess C, Miot S, Deon C, Sanchez JC, Schifferli JA. 2003. Characterisation and properties of ectosomes released by human polymorphonuclear neutrophils. *Exp Cell Res* 285:243-57.

27. Pliyev BK, Kalintseva MV, Abdulaeva SV, Yarygin KN, Savchenko VG. 2014. Neutrophil microparticles modulate cytokine production by natural killer cells. *Cytokine* 65:126-9.

28. Majumdar R, Tavakoli Tameh A, Parent CA. 2016. Exosomes mediate LTB4 release during neutrophil chemotaxis. *PLOS Biol* 14:e1002336.

29. Headland SE, Jones HR, Norling LV, Kim A, Souza PR, Corsiero E, Gil CD, Nerviani A, Dell'Accio F, Pitzalis C, Oliani SM, Jan LY, Perretti M. 2015.

Neutrophil-derived microvesicles enter cartilage and protect the joint in inflammatory arthritis. *Sci Transl Med* 7:315ra190.

30. Gasser O, Schifferli JA. 2005. Microparticles released by human neutrophils adhere to erythrocytes in the presence of complement. *Exp Cell Res* 307:381-7.

31. Nieuwland R, Berckmans RJ, McGregor S, Boing AN, Romijn FP, Westendorp RG, Hack CE, Sturk A. 2000. Cellular origin and procoagulant properties of microparticles in meningococcal sepsis. *Blood* 95:930-5.

32. Watanabe J, Marathe GK, Neilsen PO, Weyrich AS, Harrison KA, Murphy RC, Zimmerman GA, McIntyre TM. 2003. Endotoxins stimulate neutrophil adhesion followed by synthesis and release of platelet-activating factor in microparticles. *J Biol Chem* 278:33161-8.

33. Rossaint J, Kuhne K, Skupski J, Van Aken H, Looney MR, Hidalgo A, Zarbock A. 2016. Directed transport of neutrophil-derived extracellular vesicles enables platelet-mediated innate immune response. *Nat Commun* 7:13464.

34. Timar CI, Lorincz AM, Csepanyi-Komi R, Valyi-Nagy A, Nagy G, Buzas EI, Ivanyi Z, Kittel A, Powell DW, McLeish KR, Ligeti E. 2013. Antibacterial effect of microvesicles released from human neutrophilic granulocytes. *Blood* 121:510-8.

35. Hess C, Sadallah S, Hefti A, Landmann R, Schifferli JA. 1999. Ectosomes released by human neutrophils are specialized functional units. *J Immunol* 163:4564-73.

36. Lim K, Hyun Y-M, Lambert-Emo K, Capece T, Bae S, Miller R, Topham DJ, Kim M. 2015. Neutrophil trails guide influenza-specific $CD8^+$ T cells in the airways. *Science* 349.

37. Herrmann IK, Bertazzo S, O'Callaghan DJ, Schlegel AA, Kallepitis C, Antcliffe DB, Gordon AC, Stevens MM. 2015. Differentiating sepsis from non-infectious systemic inflammation based on microvesicle-bacteria aggregation. *Nanoscale* 7:13511-20.

38. Bruns S, Kniemeyer O, Hasenberg M, Aimanianda V, Nietzsche S, Thywissen A, Jeron A, Latge JP, Brakhage AA, Gunzer M. 2010. Production of extracellular traps against Aspergillus fumigatus in vitro and in infected lung tissue is dependent on invading neutrophils and influenced by hydrophobin RodA. PLoS Pathog 6:e1000873.

39. Behnsen J, Narang P, Hasenberg M, Gunzer F, Bilitewski U, Klippel N, Rohde M, Brock M, Brakhage AA, Gunzer M. 2007. Environmental dimensionality controls the interaction of phagocytes with the pathogenic fungi Aspergillus fumigatus and Candida albicans. PLoS Pathog 3:e13.

40. Jahn B, Boukhallouk F, Lotz J, Langfelder K, Wanner G, Brakhage AA. 2000. Interaction of human phagocytes with pigmentless *Aspergillus* conidia. *Infect Immun* 68:3736-9.

41. Jahn B, Langfelder K, Schneider U, Schindel C, Brakhage AA. 2002. PKSP-dependent reduction of phagolysosome fusion and intracellular kill of *Aspergillus fumigatus* conidia by human monocyte-derived macrophages. *Cell Microbiol* 4:793-803.

42. Tsai HF, Chang YC, Washburn RG, Wheeler MH, Kwon-Chung KJ. 1998. The developmentally regulated alb1 gene of *Aspergillus fumigatus*: its role in modulation of conidial morphology and virulence. *J Bacteriol* 180:3031-8.

43. Blango MG, Kniemeyer O, Brakhage AA. 2019. Conidial surface proteins at the interface of fungal infections. PLoS Pathog 15:e1007939.

44. Heinekamp T, Thywissen A, Macheleidt J, Keller S, Valiante V, Brakhage AA. 2012. Aspergillus fumigatus melanins: interference with the host endocytosis pathway and impact on virulence. Front Microbiol 3:440.

45. Yanez-Mo M, Siljander PR, Andreu Z, Zavec AB, Borras FE, Buzas EI, Buzas K, Casal E, Cappello F, Carvalho J, Colas E, Cordeiro-da Silva A, Fais S, Falcon-Perez JM, Ghobrial IM, Giebel B, Gimona M, Graner M, Gursel I, Gursel M, Heegaard NH, Hendrix A, Kierulf P, Kokubun K, Kosanovic M, Kralj-Iglic V, Kramer-Albers EM, Laitinen S, Lasser C, Lener T, Ligeti E, Line A, Lipps G, Llorente A, Lotvall J, Mancek-Keber M, Marcilla A, Mittelbrunn M, Nazarenko I, Nolte-'t Hoen EN, Nyman TA, O'Driscoll L, Olivan M, Oliveira C, Pallinger E, Del Portillo HA, Reventos J, Rigau M, Rohde E, Sammar M, et al. 2015. Biological properties of extracellular vesicles and their physiological functions. *J Extracell Vesicles* 4:27066.

46. Krogh A, Larsson B, von Heijne G, Sonnhammer EL. 2001. Predicting transmembrane protein topology with a hidden Markov model: application to complete genomes. J Mol Biol 305:567-80.

47. Petersen TN, Brunak S, von Heijne G, Nielsen H. 2011. SignalP 4.0: discriminating signal peptides from transmembrane regions. Nat Methods 8:785-6.

48. Horton P, Park KJ, Obayashi T, Fujita N, Harada H, Adams-Collier CJ, Nakai K. 2007. WoLF PSORT: protein localization predictor. *Nucleic Acids Res* 35:W585-7.

49. Ruf D, Brantl V, Wagener J. 2018. Mitochondrial Fragmentation in Aspergillus fumigatus as Early Marker of Granulocyte Killing Activity. Front Cell Infect Microbiol 8:128.

50. Tkalcevic J, Novelli M, Phylactides M, Iredale JP, Segal AW, Roes J. 2000. Impaired immunity and enhanced resistance to endotoxin in the absence of neutrophil elastase and cathepsin G. *Immunity* 12:201-10.

51. Newman SL, Gootee L, Gabay JE, Selsted ME. 2000. Identification of constituents of human neutrophil azurophil granules that mediate fungistasis against Histoplasma capsulatum. Infect Immun 68:5668-72.

52. Gazendam RP, van de Geer A, Roos D, van den Berg TK, Kuijpers TW. 2016. How neutrophils kill fungi. *Immunol Rev* 273:299-311.

53. Langfelder K, Jahn B, Gehringer H, Schmidt A, Wanner G, Brakhage AA. 1998. Identification of a polyketide synthase gene (pksP) of *Aspergillus fumigatus* involved in conidial pigment biosynthesis and virulence. Med Microbiol Immunol 187:79-89.

54. Jahn B, Koch A, Schmidt A, Wanner G, Gehringer H, Bhakdi S, Brakhage AA. 1997. Isolation and characterization of a pigmentless-conidium mutant of *Aspergillus fumigatus* with altered conidial surface and reduced virulence. Infect Immun 65:5110-7.

55. Langfelder K, Philippe B, Jahn B, Latge JP, Brakhage AA. 2001. Differential expression of the *Aspergillus fumigatus pksP* gene detected *in vitro* and *in vivo* with green fluorescent protein. Infect Immun 69:6411-8.

56. Ellett F, Jorgensen J, Frydman GH, Jones CN, Irimia D. 2017. Neutrophil Interactions Stimulate Evasive Hyphal Branching by Aspergillus fumigatus. PLoS Pathog 13:e1006154.

57. Genschmer KR, Russell DW, Lal C, Szul T, Bratcher PE, Noerager BD, Abdul Roda M, Xu X, Rezonzew G, Viera L, Dobosh BS, Margaroli C, Abdalla TH, King RW, McNicholas CM, Wells JM, Dransfield MT, Tirouvanziam R, Gaggar A, Blalock JE. 2019. Activated PMN Exosomes: Pathogenic Entities Causing Matrix Destruction and Disease in the Lung. Cell 176:113-126 e15.

58. Lother J, Breitschopf T, Krappmann S, Morton CO, Bouzani M, Kurzai O, Gunzer M, Hasenberg M, Einsele H, Loeffler J. 2014. Human dendritic cell subsets display distinct interactions with the pathogenic mould *Aspergillus fumigatus*. *Int J Med Microbiol* 304:1160-8.

59. Weidner G, d'Enfert C, Koch A, Mol PC, Brakhage AA. 1998. Development of a homologous transformation system for the human pathogenic fungus *Aspergillus fumigatus* based on the *pyrG* gene encoding orotidine 5'-monophosphate decarboxylase. Curr Genet 33:378-85.

60. Lorincz AM, Timar CI, Marosvari KA, Veres DS, Otrokocsi L, Kittel A, Ligeti E. 2014. Effect of storage on physical and functional properties of extracellular vesicles derived from neutrophilic granulocytes. *J Extracell Vesicles* 3:25465.

61. Wessel D, Flugge UI. 1984. A method for the quantitative recovery of protein in dilute solution in the presence of detergents and lipids. Anal Biochem 138:141-3.

62. Baldin C, Valiante V, Kruger T, Schafferer L, Haas H, Kniemeyer O, Brakhage AA. 2015. Comparative proteomics of a tor inducible *Aspergillus fumigatus* mutant reveals involvement of the Tor kinase in iron regulation. *Proteomics* 15:2230-43.

63. Dorfer V, Pichler P, Stranzl T, Stadlmann J, Taus T, Winkler S, Mechtler K. 2014. MS Amanda, a universal identification algorithm optimized for high accuracy tandem mass spectra. *Journal of Proteome Research* 13:3679-3684.

64. Vizcaino JA, Csordas A, del-Toro N, Dianes JA, Griss J, Lavidas I, Mayer G, Perez-Riverol Y, Reisinger F, Ternent T, Xu QW, Wang R, Hermjakob H. 2016. 2016 update of the PRIDE database and its related tools. *Nucleic Acids Res* 44:D447-56.

65. Piper RC, Katzmann DJ. 2007. Biogenesis and function of multivesicular bodies. *Annual review of cell and developmental biology* 23:519-547.

66. Ihaka R, Gentleman R. 1996. R: a language for data analysis and graphics. *Journal of Computational and Graphical Statistics* 5:299-314.

67. Priebe S, Kreisel C, Horn F, Guthke R, Linde J. 2015. FungiFun2: a comprehensive online resource for systematic analysis of gene lists from fungal species. *Bioinformatics* 31:445-446.

68. Helmschrott C, Sasse A, Samantaray S, Krappmann S, Wagener J. 2013. Upgrading fungal gene expression on demand: improved systems for

doxycycline-dependent silencing in *Aspergillus fumigatus*. Applied and environmental microbiology 79:1751-1754.

69. Unkles SE, Valiante V, Mattern DJ, Brakhage AA. 2014. Synthetic biology tools for bioprospecting of natural products in eukaryotes. Chem Biol 21:502-508.

Figure Captions

FIG 1

***A. fumigatus* induces EVs release by human neutrophils.** (A) Time course of apoptotic body occurrence (green lines) and fungal-induced cell death (teal lines) at MOI 5 and 10. n = 10(15) and n = 12(17) for apoptotic body counts for MOI 5 and 10, respectively. n = 4(20) and n = 5(15) for viability data for MOI 5 and MOI 10, respectively. (B) Percentage of apoptotic bodies per total number of EVs. (C-E) Time course of total EV release and EV surface markers (C) Annexin V, (D) CD11b, and (E) CD63. sEVs were collected from uninfected cells. Symbols represent significant differences between *pksP* EVs and afEVs (*), *pksP* EVs and sEVs (+), afEVs and sEVs (x). (C) n = 27(40) for sEVs, n = 16 for afEVs and *pksP* EVs; (D) n = 23 for sEVs, n = 16 for afEVs and *pksP* EVs; (E) n = 13 for sEVs, n = 9 for afEVs and *pksP* EVs. Data in (A and B-E) are presented as medians and interquartile range of absolute numbers of EVs per 10^7 PMNs. * $p < 0.05$, ** $p < 0.01$, *** $p < 0.001$ (Mann-Whitney test). (F-M) Cryo-TEM images of sEVs (F-I) and afEVs (J-M) 2 h post interaction. Representative images displaying sEVs (G-I) and afEVs (K-M) with different appearance. Scale bars correspond to 200 nm.

FIG 2

Analysis of the EV proteome by LC-MS/MS reveals that neutrophil-derived EVs retain a core proteome cargo after infection. (A) Venn diagram (Venny 2.1.0 software) indicating overlap of proteins identified from each EV population using label-free quantification. (B-D) Volcano plots comparing proteins identified in afEVs, *pksP* EVs, and sEVs using the LFQ-based proteomics method.

FIG 3

afEVs elicit fungistatic effects on wt fungus. (A) Representative bright field images after 10 h of incubation of wt fungal hyphae with afEVs and *pksP* EVs. Single (1×) or triple (3×) doses of EVs were applied. (B-E) Growth of wt fungal hyphae after 10 h of coincubation with afEVs and *pksP* EVs derived from four different donors. The size of hyphae was assessed by automated analysis of 2D image data and results are displayed as median hyphae area in μm^2 in each field of view; data are represented as medians and interquartile range of the median hyphae area in each field of view; n = 10 fields of view per condition per time point. (F) Representative growth curves of wt fungal strain in presence and absence of EVs for donor shown in (D). (G) Effects of sEVs on wt conidia compared to those of afEVs on wt conidia, n = 3 independent experiments, 20 fields of view per experiment per condition. * $p < 0.05$, ** $p < 0.01$, *** $p < 0.001$, **** $p < 0.0001$ (Mann-Whitney test).

FIG 4

Effect of afEVs on hyphae. (A) Density of afEVs and *pksP* EVs inside and outside of wt and *pksP* mutant hyphae. (B) The fraction of PI-stained hyphae indicates permeable fungal hyphae and provides an estimation of hyphae-associated DNA signals in wt and *pksP* hyphae treated with afEVs and *pksP* EVs, respectively, compared to untreated control hyphae. Data in (A) and in (B) for EV groups derived

from 3 independent experiments (n = 13 and 21 technical replicates for *pksP* and wt, respectively). Data in (B) for controls are representative of 1 experiment (n = 5 technical replicates). * $p < 0.05$, ** $p < 0.01$, *** $p < 0.001$ (Mann-Whitney test). (C) SEM of 50 h old cultures of wt (lower panel) treated with afEVs vs. healthy hyphae grown alone (upper panel). Samples were immobilized on filter membranes with a defined pore size of 5 µm (black circles). Scale bars are 50 µm. SEM images represent observations from two independent experiments with three technical replicates.

FIG 5

afEVs kill fungal hyphae. AfS35 pJW103 hyphae expressing a mitochondrial GFP reporter (green) grown for 20 h were stained with calcofluor white (blue) and incubated with sEVs, afEVs, *pksP* EVs, 3 mM H_2O_2 as a positive control for cell death induction, or left untreated and then monitored by CLSM. A healthy filamentous mitochondrial network is shown in green in an untreated sample. A fragmented mitochondrial network indicates cell death as seen when 3 mM H_2O_2 was used as a positive control for cell death. Images are representative of four separate experiments with different donors. Scale bars are 10 µm.

FIG 6

afEVs are internalized into the fungal cell wall and cytoplasm. afEV internalization into fungi was analyzed by 3D quantitative analysis of Z-stacks with GFP-expressing *A. fumigatus* after 20 h of co-incubation. (A,B) Representative cross-sections of Z-stacks showing lateral (X and Y) and axial (Z) dimensions of (A) a hyphae with internalized afEVs in red (Alexa-647), fungal cell wall in blue (calcofluor

white), and fungal cytoplasm in green (GFP) and corresponding control hyphae shown in (B). Scale bars represent 2 µm. Image intensity was inverted. The darkest color corresponds to the highest fluorescence intensity. Histograms display specificity of signal of Alexa 647 dye used to stain afEVs. As seen in the control Z-stack, there is unspecific Alexa staining likely due to dye aggregation. (C) Schematic diagram of a cross-section of hyphae and different stages of afEV internalization. afEVs were located in 4 areas as indicated by the graphical representation. (D) Overview from the 3D image analysis of different locations of afEVs. Data are representative of 3 independent experiments with a total of 25 Z-stacks.

FIG 7

Intracellular production of human azurocidin and cathepsin G proteins is toxic to *A. fumigatus.* (A) *A. fumigatus* wt and mutant strains Afazuro, AfcathG, and AfRBP7 harboring the human azurocidin, cathepsin G and *RBP7* gene, respectively, under the control of the tet^{ON} promoter. Cultures were grown for 24 h in the absence or presence of doxycycline. (B) Biomass measurement of wt and *A. fumigatus* mutant strains Afazuro, AfcathG, and AfRBP7 with and without doxycycline. Data are representative of 3 independent experiments with three technical replicates. * $p < 0.05$, ** $p < 0.01$, *** $p < 0.001$ (Mann-Whitney test). (C) Detection of produced proteins in the *A. fumigatus* mutant strains. Bar plot shows the abundance level of the azurocidin protein in the case of the Afazuro strain, cathepsin G protein for AfcathG strain, and RBP7 for the AfRBP7 strain based on the intensity of the precursor ion. Data are generated from three analytical replicates.

Supporting Information

FIG S1

Flow cytometry analysis of PMN-derived EVs. (A) Purity of human PMNs used to generate PMN-derived EVs. Purity was assessed by flow cytometry based on staining for $CD66b^+CD16b^+$ PMNs, $CCR3^+$ eosinophils, $CD14^+$ monocytes, $CD3^+$ T cells, $CD19^+$ B cells, $CD56^+$ NK, and NKT cells. The predominant contaminating fraction of cells were eosinophils. (B-C) Analysis of apoptotic bodies defined as double positive Annexin V^+/PI^+ EVs. PMNs cultured for 3 days on DMEM medium at 37ºC were used as positive control for apoptosis (left panel). Two donors are shown in the center and right panel. (D-E) Flow cytometry protocol for phenotyping afEVs. (D) The instrumental background noise by pure HBSS is recorded and subsequently subtracted from all samples. (E) Mid-intensity rainbow beads of size 3.8 µm are recorded to set the upper detection limit; afEVs are detected in the gate above the noise and below the beads in (E). Single-stained afEVs with the corresponding isotype Abs were used as negative controls in (F) and (G). Stained afEV suspensions were measured before (F) and after (G) detergent treatment with 1% (v/v) Triton X-100 to verify the vesicular nature of detected events. False positive events (detergent resistant) are subtracted from the results

FIG S2

Characterization of afEV surface markers by flow cytometry. (A) Flow cytometry measurement of PMN surface marker dynamics of CD11b and CD63 during infection with wt and *pksP* conidia at an MOI 5. PMNs were gated according to FSC/SSC properties, dead cells were excluded by staining with viability Zombie Dye, and expression of CD11b and CD63 was analyzed with FlowJo software (Tree Star). (B) Size distribution of afEVs, *pksP* EVs, and sEVs generated at different time points measured by dynamic light scattering. Data are representative of 3 independent

experiments. (C) The time course of apoptotic body occurrence (green lines) compared to that of fungus-induced cell death (teal lines) for wt and *pksP* infected PMNs. Data are represented as medians and interquartile range. Data for EVs are shown as absolute or relative vesicle numbers per 10^7 PMNs. * $p < 0.05$, ** $p < 0.01$, *** $p < 0.001$ (Mann-Whitney test). (D) Opsonization of wt and *pksP* mutant conidia as determined by flow cytometry for C3 immunofluorescence staining. Bars indicate mean fluorescence intensity plus standard deviation of two experiments with 5 replicates each.

FIG S3

Neutrophil EV composition differs depending on the stimuli. (A-C) Volcano plots comparing proteins identified in afEV, *pksP* EV, and sEVs using the TMT-labeling proteomics method. (D) Gene Ontology (GO)-term enrichment analysis of the core proteome cargo (60 proteins) based on FungiFun2 tool reveals pathways of EV biogenesis. Data are representative of 2 technical replicates.

FIG S4

Effect of afEVs on *pksP* mutant fungal cells. (A) Segmentation steps of an automated algorithm for 2D image analysis of fungal growth with (top rows) and without (bottom rows) afEVs. Scale bars are 20 µm. (B) Representative bright field images after 10 h of incubation of fungi with afEVs and *pksP* EVs on *pksP* mutant hyphae. Untreated hyphae received no EVs. Single (1×) or triple (3×) doses of EVs were applied as described in the methods. (C-F) Growth of *pksP* mutant fungal hyphae after 10 h of coincubation with afEVs and *pksP* EVs derived from four different donors. The size of hyphae was assessed by automated analysis of 2D image data and results are displayed as median hyphae area in μm^2 in each field of

view; data are represented as medians and interquartile range of the median hyphae area in each field of view; n = 10 fields of view per condition per time point. (G) Representative growth curves of *pksP* fungal strain in presence and absence of EVs for donor shown in (E).

FIG S5

Testing of hyphae and EV volume. Equal volumes of (A) EVs and (B) hyphae for wt and *pskP* samples were analyzed. (C) Dependence of the volume fraction of the hyphae-associated afEVs (volume of hyphae-associated afEVs divided by the total afEV volume) on the volume concentration of afEVs (total afEV volume divided by the sample volume). (D) Dependence of the volume fraction of hyphae-associated EVs on the volume concentration of hyphae (hyphae volume divided by the sample volume). (E) Dependence of the volume fraction of the hyphae-associated DNA (HADNA) that interacts with EVs on the volume fraction of hyphae-associated EVs.

FIG S6

SEM imaging of afEV-treated hyphae. SEM of 50 h old cultures of wt hyphae (lower panel) treated with afEVs *vs.* healthy hyphae grown alone (upper panel). Samples were immobilized on filter membranes with a defined pore size of 5 µm (as seen in the overview images). The scale bar on the far-right panels is 1 µm. Scale bars on all other images are 5 µm. SEM images represent observations from 3 technical replicates, two independent experiments.

FIG S7

Verification of *A. fumigatus* transgenic strains expressing human EV proteins. (A) Schematic of the predicted *Bam*HI restriction sites in the genome of the mutant

strains following integration of the constructs used to express the human genes in the parental strain. tet^{ON} promoter, azurocidin-encoding gene, cathepsin G-encoding gene, RBP7-encoding gene, *tef* terminator, *ptrA* cassette (pyrithiamine resistance marker). (B) Southern blot for confirmation of construct integration into the *A. fumigatus* genome. In the transgenic strains, a band with the expected size of 1.7 kb for the Afazuro strain, 1.4 kb for the AfcathG strain, and 1.4 kb for the AfRBP7 strain were observed. No signal was detected for the non-transformed wt strain.

File S1

Tables S1-S4. Table S1: Identified proteins with transmembrane domains predicted by SignalP, TMHMM and WoLF PSORT based on the here obtained TMT and LFQ data sets; Table S2: Twenty most abundant proteins (PSMs/AAs) by TMT quantitation. Table S3: Twenty most abundant proteins (PSMs/AAs) by label-free quantitation. Table S4: List of primers used in this study.

Movie S1

Movie generation by using different dyes and reconstruction. The video shows 3D surface reconstructions for image-based analysis of the interaction of afEVs with *A. fumigatus*. CLSM Z-stacks were captured 20 h post interaction. Cell wall chitin structures were stained with calcofluor white (blue channel). DNA was stained with PI (red channel). afEVs were stained with Annexin-V-FITC (green channel).

Movie S2

afEVs localize to four regions including the fungal cell wall and cytoplasm The video shows 3D surface reconstructions for image-based analysis of the interaction of afEVs with *A. fumigatus*. CLSM Z-stacks were captured 20 h post interaction. Cell

wall chitin structures were stained with calcofluor white (blue channel). afEVs were stained with with Annexin-V Alexa 647 (red channel). The fungal cytoplasm contained eGFP (green channel).

Movie S3

Hyphae respond to afEVs by hyperbranching away from afEVs The video shows 3D surface reconstructions for image-based analysis of the interaction of afEVs with *A. fumigatus*. CLSM Z-stacks were captured 20 h post interaction. Cell wall chitin structures were stained with calcofluor white (blue channel). DNA was stained with PI (red channel). afEVs were stained with Annexin-V-FITC (green channel).

Figure 1

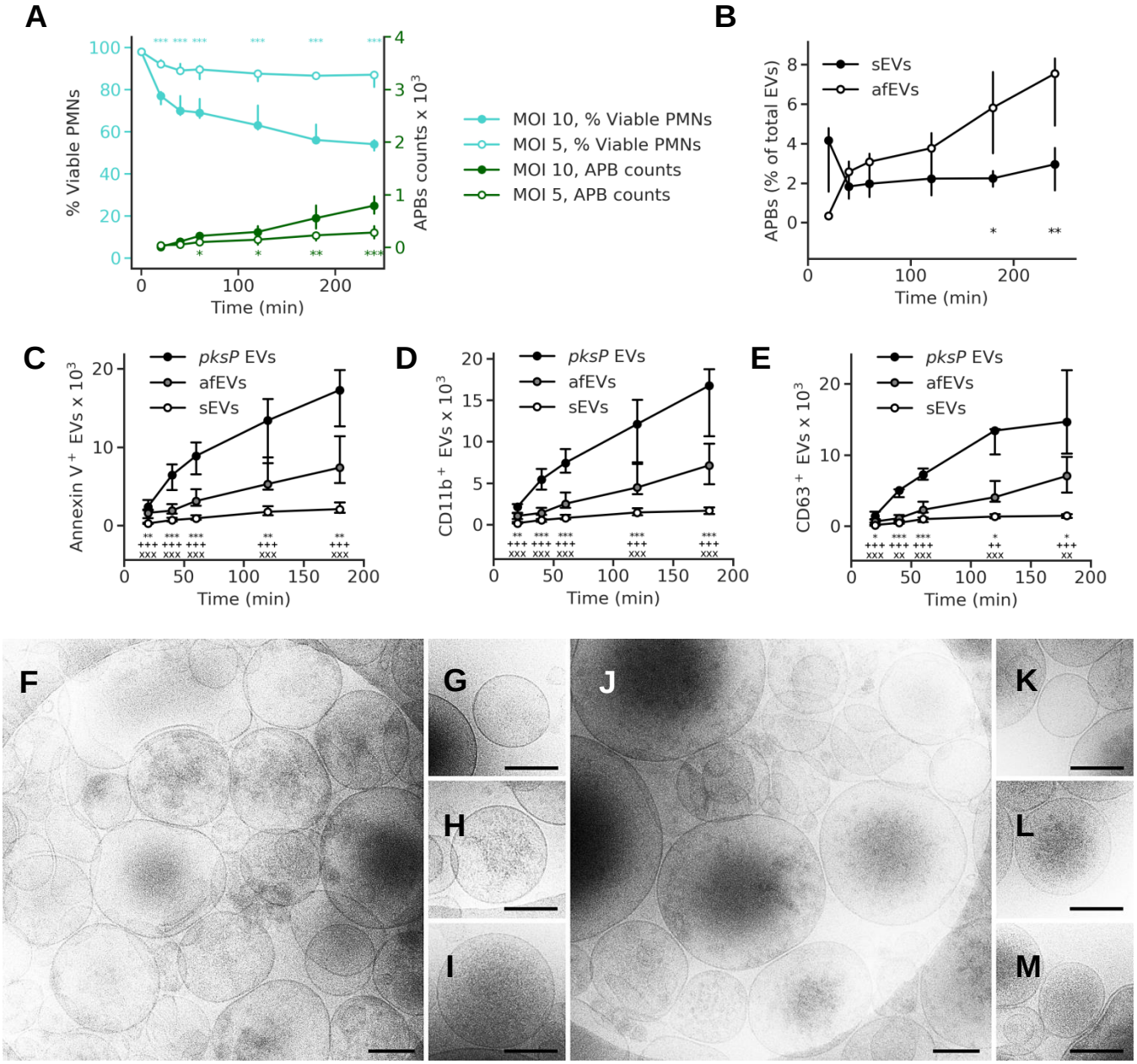
A
% Viable PMNs
APBs counts x 10³
Time (min)
MOI 10, % Viable PMNs
MOI 5, % Viable PMNs
MOI 10, APB counts
MOI 5, APB counts
B
APBs (% of total EVs)
sEVs
afEVs
Time (min)
C
Annexin V⁺ EVs x 10³
pksP EVs
afEVs
sEVs
Time (min)
D
CD11b⁺ EVs x 10³
pksP EVs
afEVs
sEVs
Time (min)
E
CD63⁺ EVs x 10³
pksP EVs
afEVs
sEVs
Time (min)
F
G
H
I
J
K
L
M

Figure 2

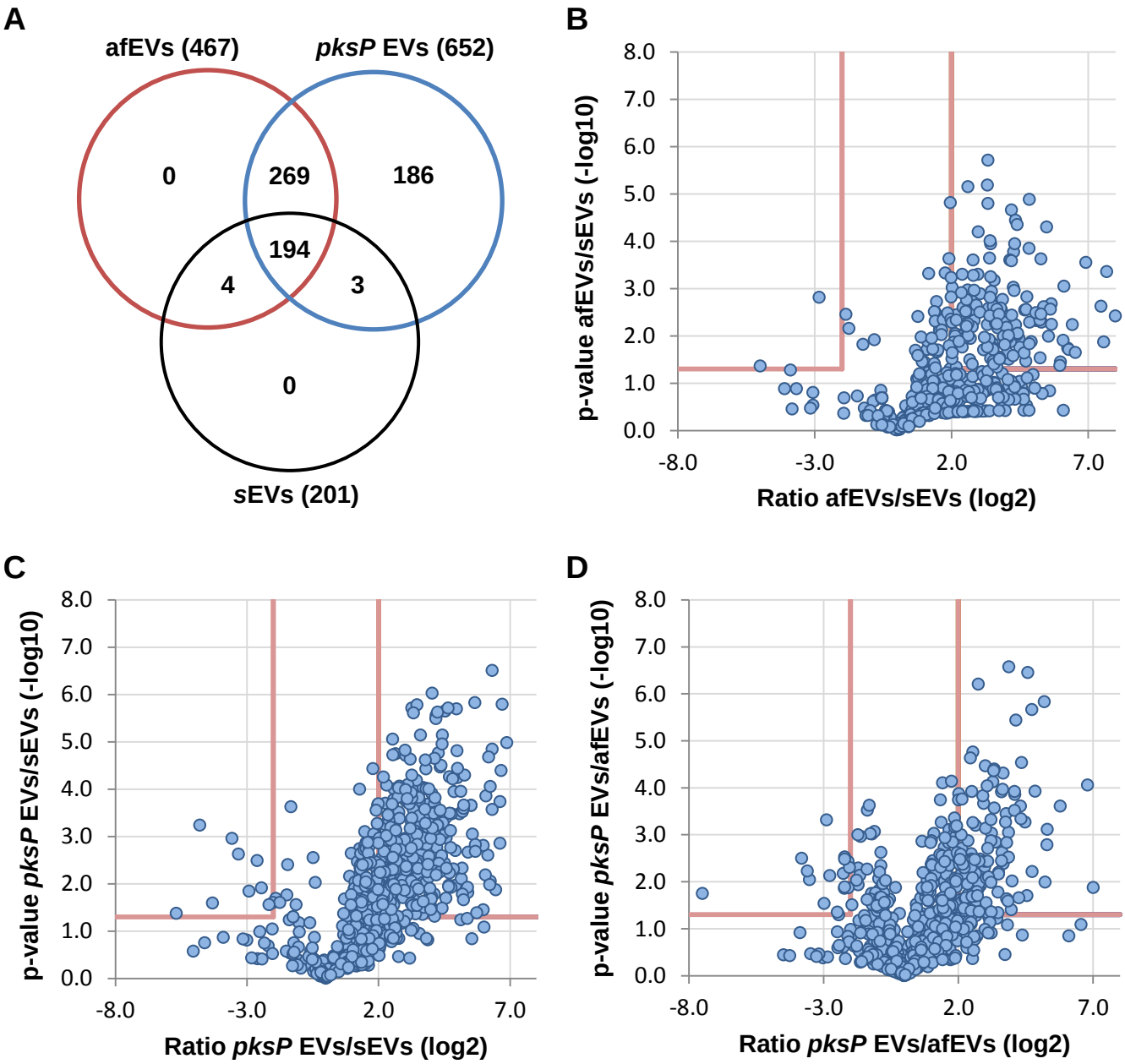
A
afEVs (467)
pksP EVs (652)
0
269
186
194
4
3
0
sEVs (201)
B
p-value afEVs/sEVs (-log10)
Ratio afEVs/sEVs (log2)
C
p-value pksP EVs/sEVs (-log10)
Ratio pksP EVs/sEVs (log2)
D
p-value pksP EVs/afEVs (-log10)
Ratio pksP EVs/afEVs (log2)
8.0
7.0
6.0
5.0
4.0
3.0
2.0
1.0
0.0
-8.0
-3.0
2.0
7.0

Figure 3

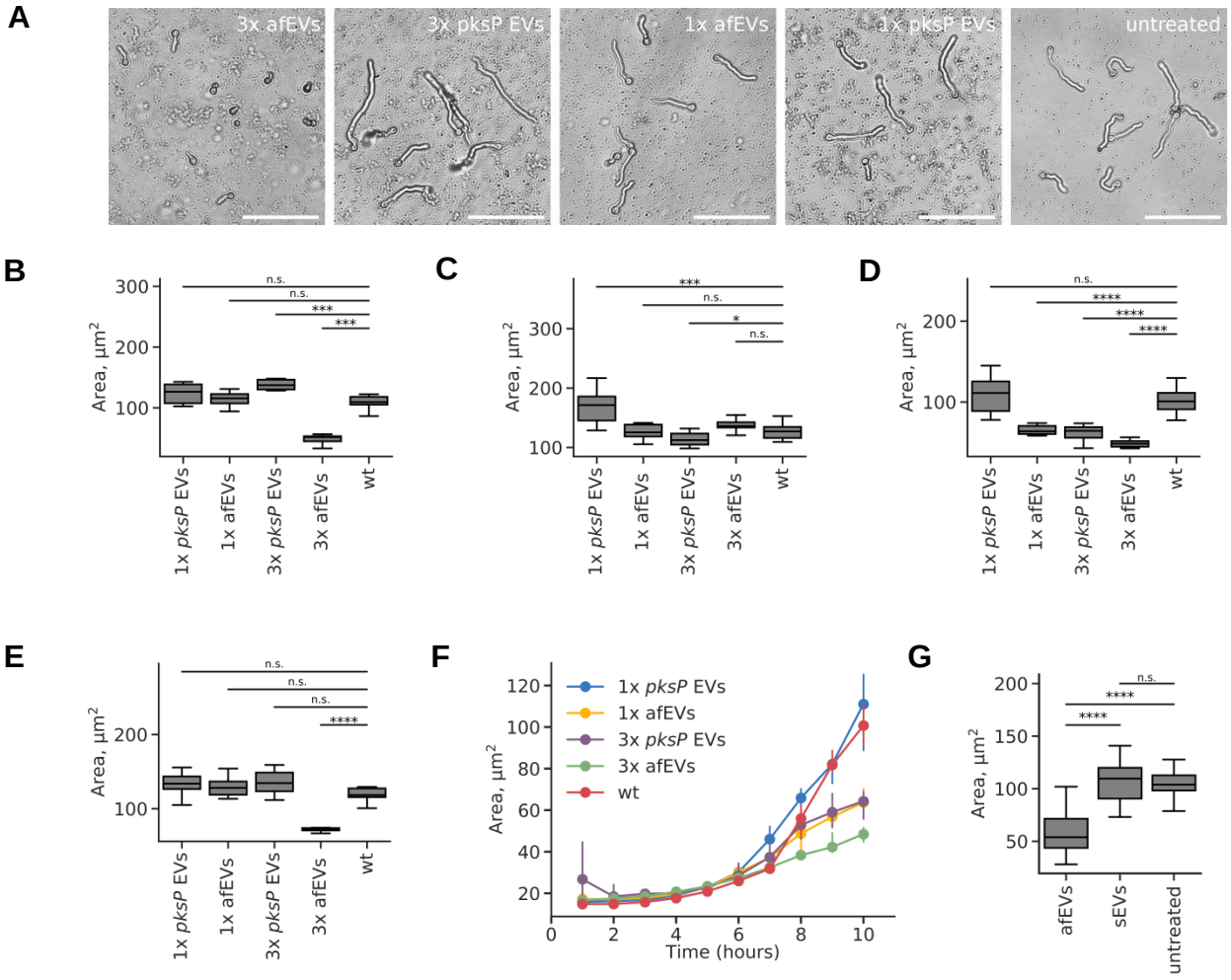
A
3x afEVs
3x pksP EVs
1x afEVs
1x pksP EVs
untreated
B
C
D
E
F
G
Area, µm²
1x pksP EVs
1x afEVs
3x pksP EVs
3x afEVs
wt
n.s.
***
*
****
Time (hours)
afEVs
sEVs
untreated

Figure 4

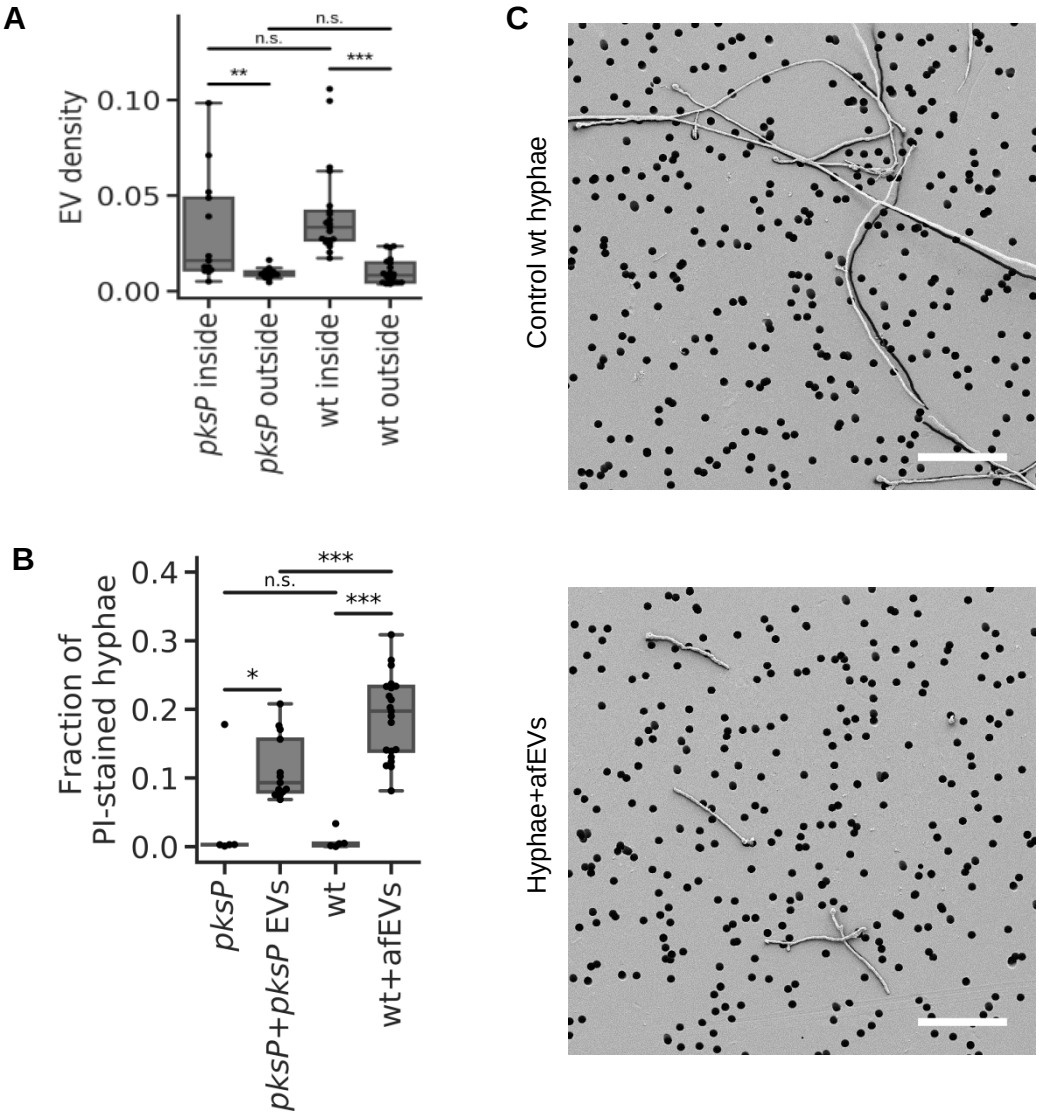
A
EV density
0.10
0.05
0.00
n.s.
n.s.
**
***
pksP inside
pksP outside
wt inside
wt outside
B
Fraction of PI-stained hyphae
0.4
0.3
0.2
0.1
0.0
***
n.s.
***
*
pksP
pksP+pksP EVs
wt
wt+afEVs
C
Control wt hyphae
Hyphae+afEVs

Figure 5

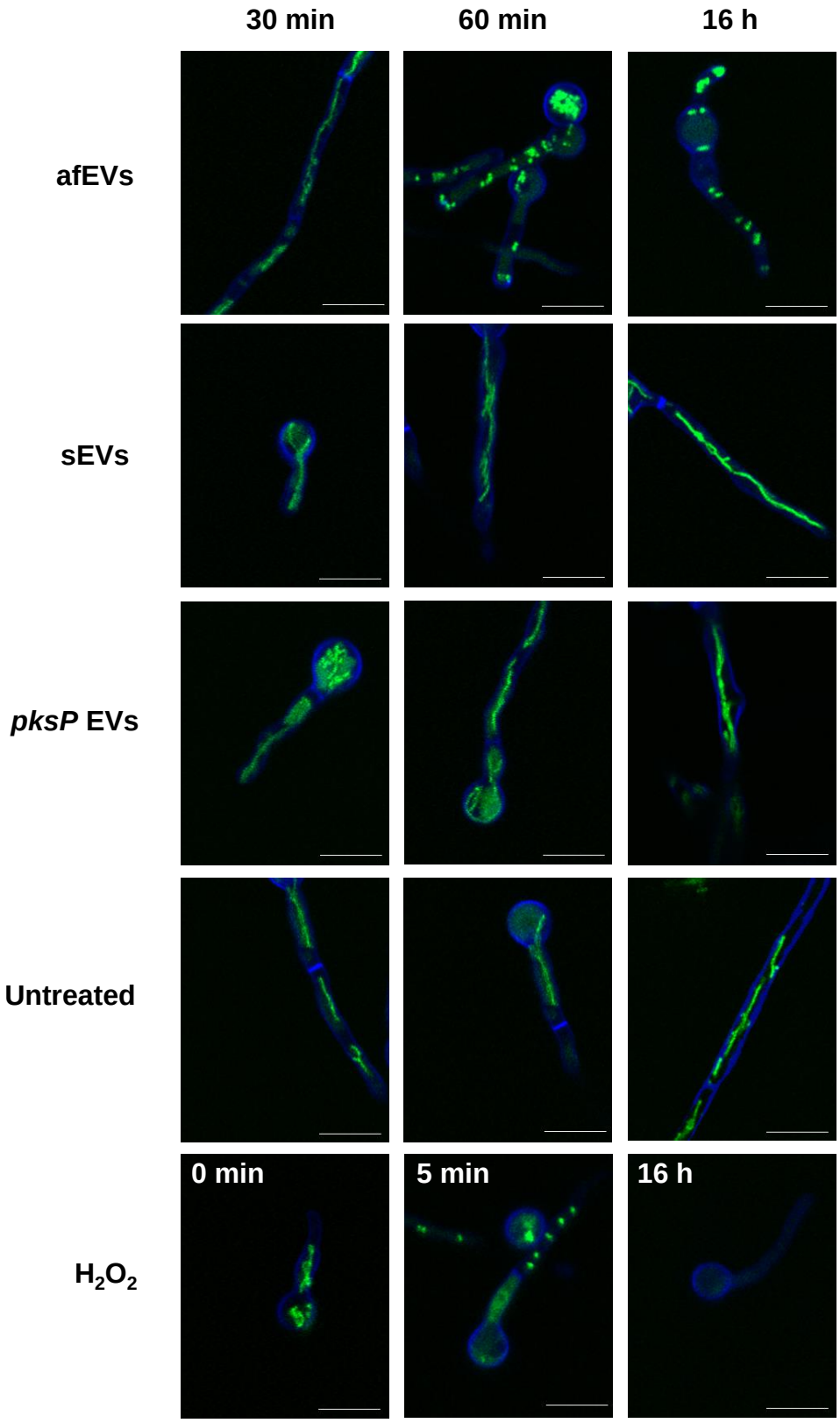
30 min
60 min
16 h
afEVs
sEVs
pksP EVs
Untreated
0 min
5 min
16 h
H2O2

Figure 6

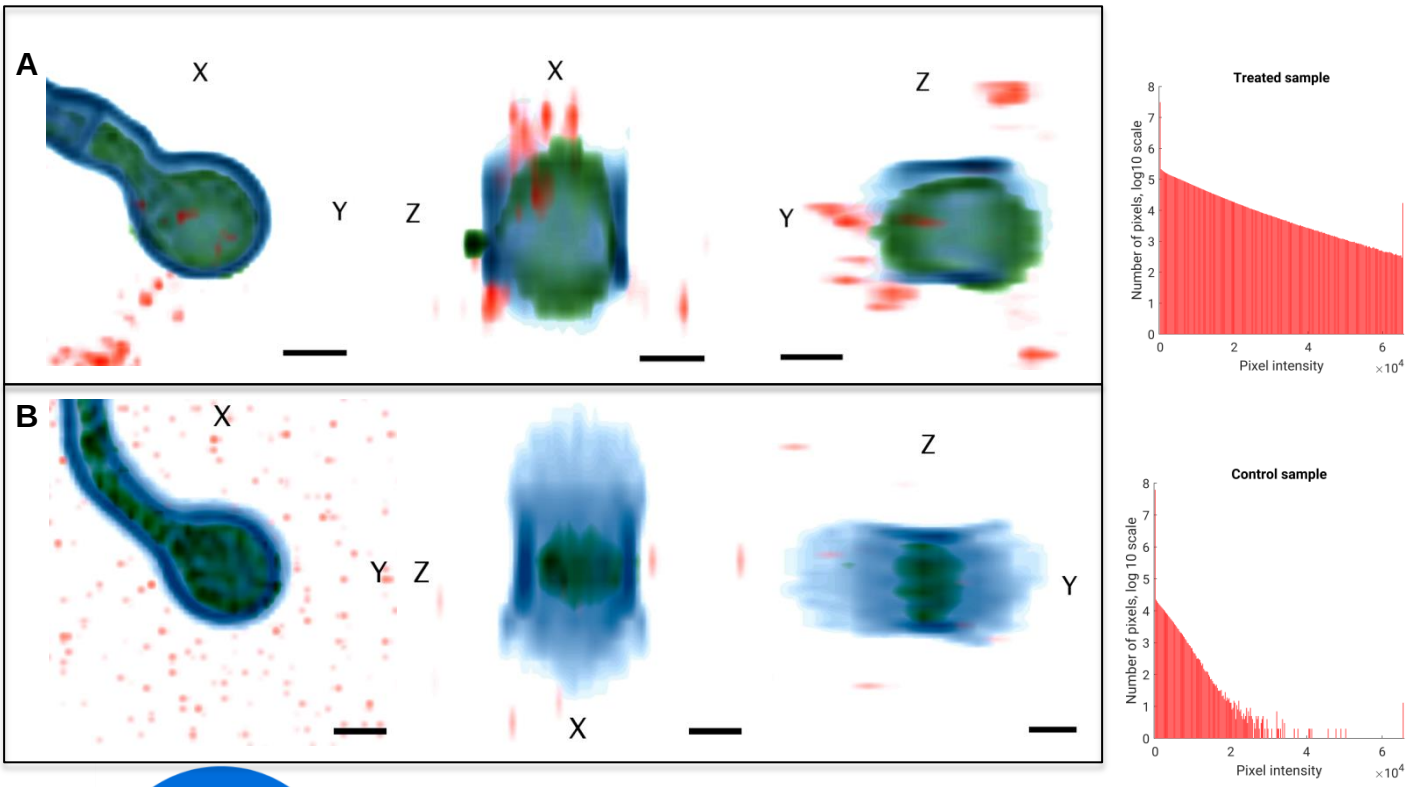

C

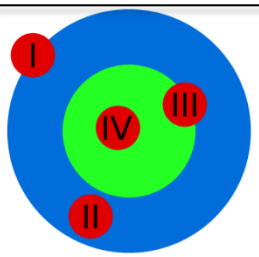

Type I afEVs - **cell wall-associated**

Type II afEVs - **cell wall-embedded**

Type III afEVs - **embedded at cell wall/cytoplasm interface**

Type IV afEVs - **intracytoplasmic**

D

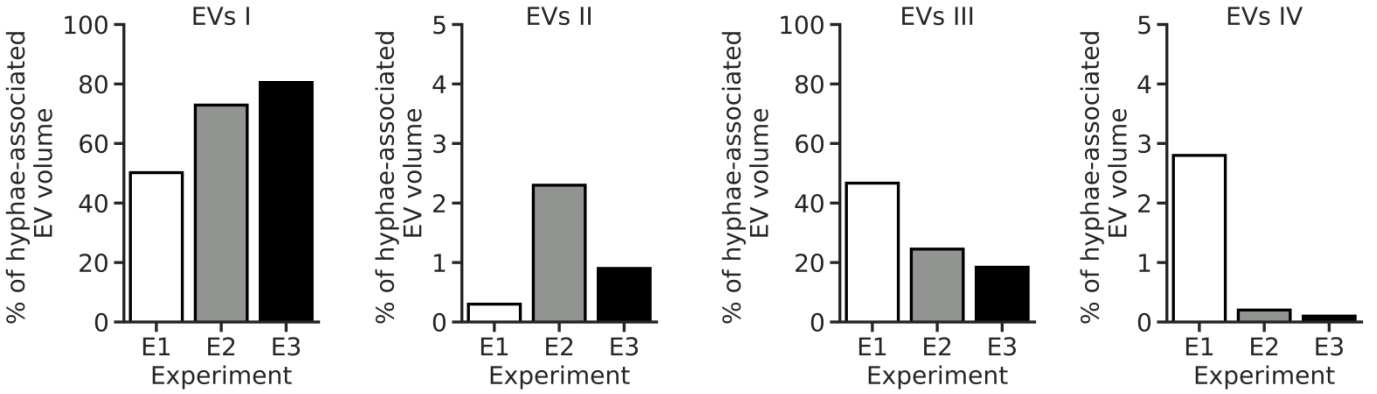

Figure 7

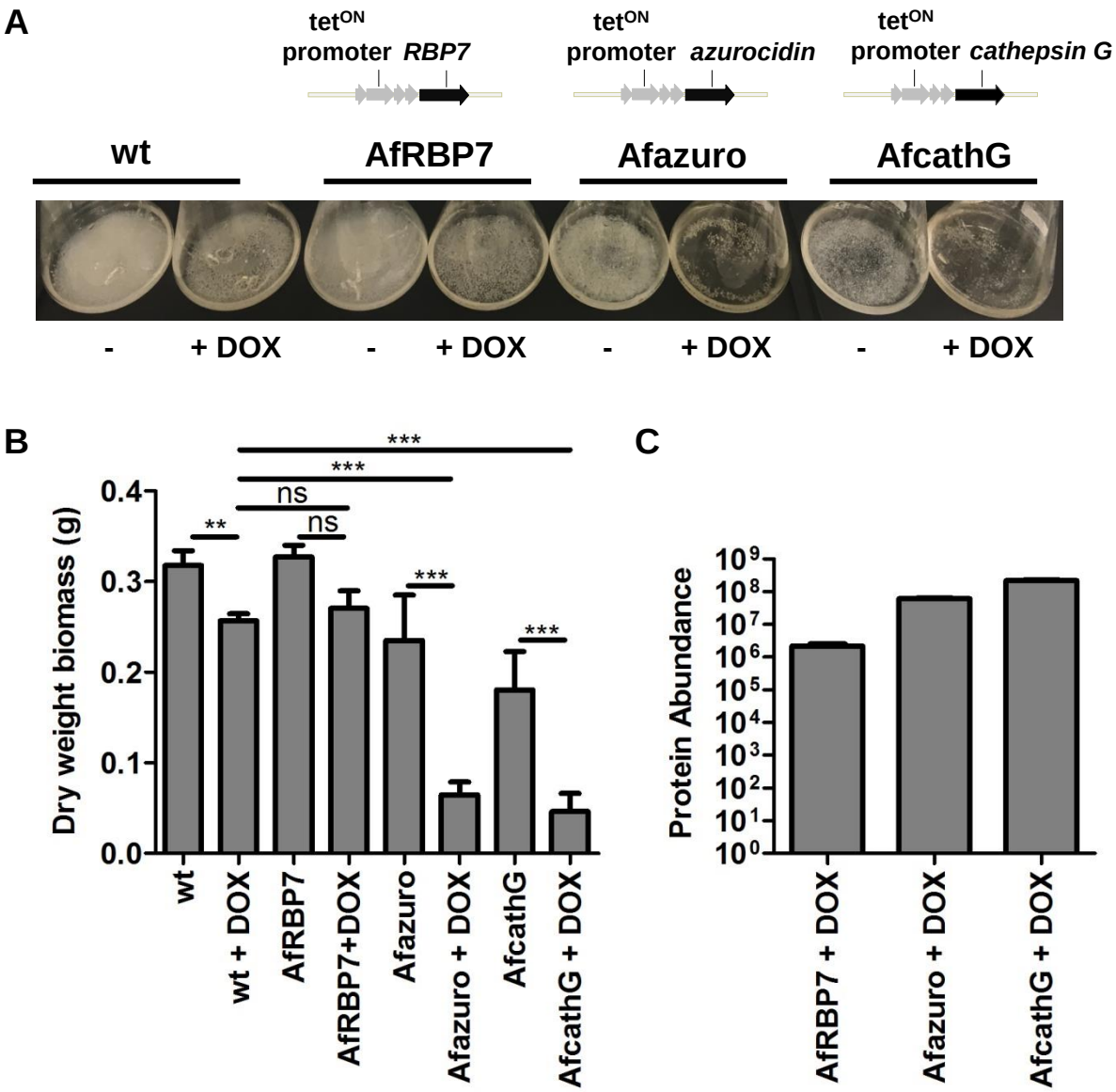
A
tetON promoter RBP7
tetON promoter azurocidin
tetON promoter cathepsin G
wt
AfRBP7
Afazuro
AfcathG
- + DOX - + DOX - + DOX - + DOX
B
Dry weight biomass (g)
0.4
0.3
0.2
0.1
0.0
**
ns
ns
***
***
***
***
wt
wt + DOX
AfRBP7
AfRBP7+DOX
Afazuro
Afazuro + DOX
AfcathG
AfcathG + DOX
C
Protein Abundance
10^9
10^8
10^7
10^6
10^5
10^4
10^3
10^2
10^1
10^0
AfRBP7 + DOX
Afazuro + DOX
AfcathG + DOX

Figure S1

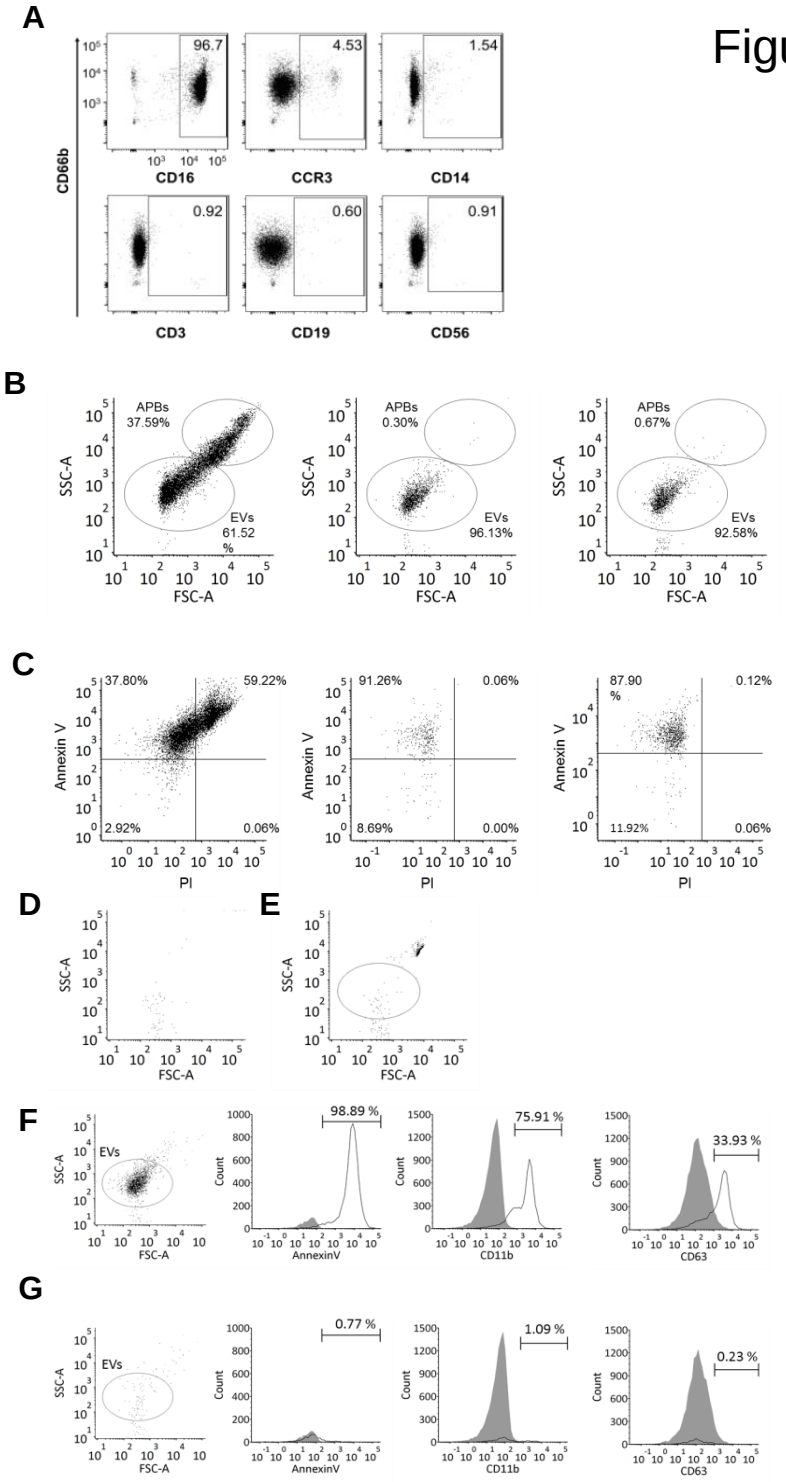
A
CD66b
96.7
4.53
1.54
CD16
CCR3
CD14
0.92
0.60
0.91
CD3
CD19
CD56
B
APBs 37.59%
EVs 61.52 %
APBs 0.30%
EVs 96.13%
APBs 0.67%
EVs 92.58%
SSC-A
FSC-A
C
37.80%
59.22%
2.92%
0.06%
91.26%
0.06%
8.69%
0.00%
87.90 %
0.12%
11.92%
0.06%
Annexin V
PI
D
E
SSC-A
FSC-A
F
EVs
98.89 %
75.91 %
33.93 %
Count
AnnexinV
CD11b
CD63
G
EVs
0.77 %
1.09 %
0.23 %

Figure S2

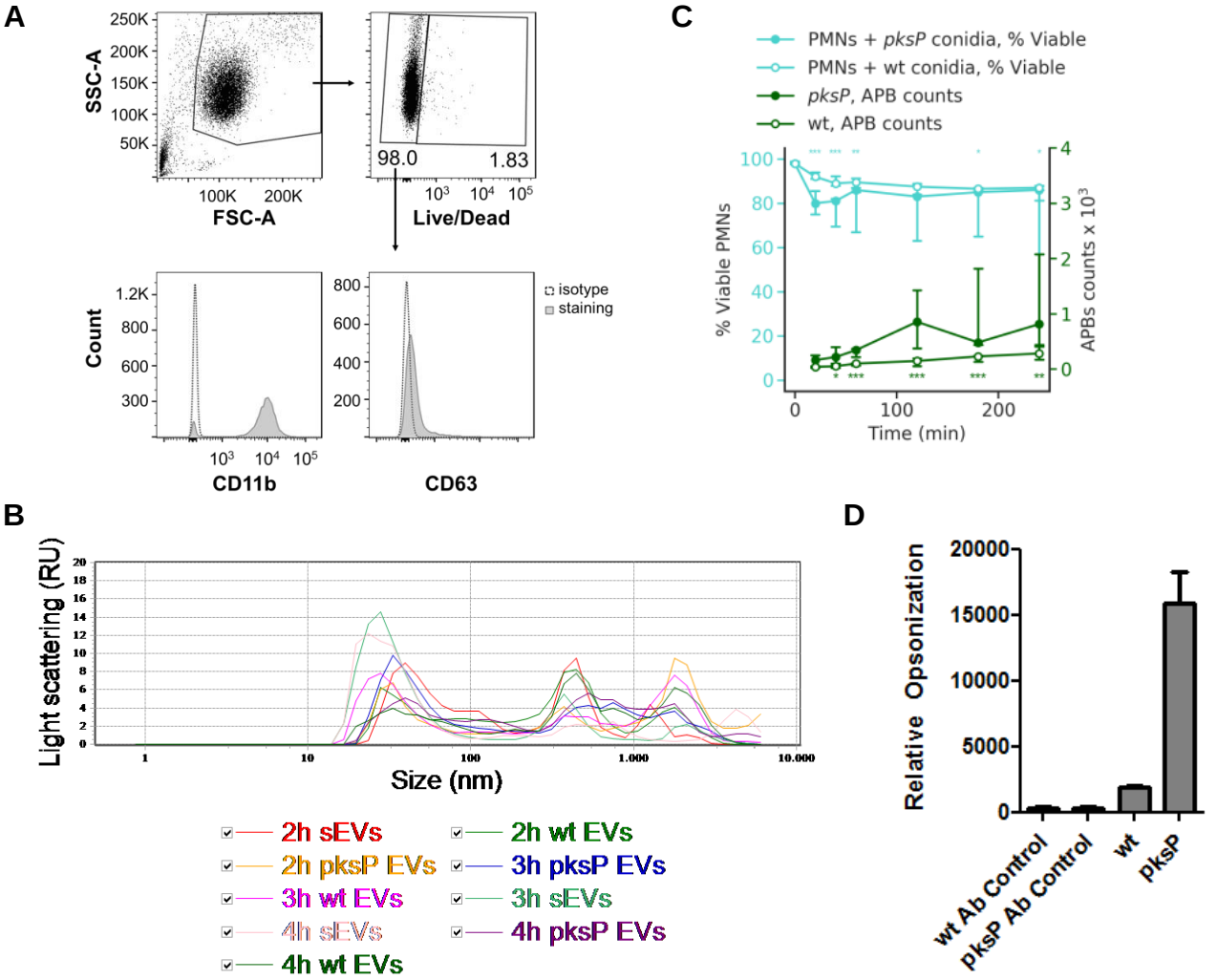
A
SSC-A
FSC-A
Live/Dead
98.0
1.83
Count
CD11b
CD63
isotype
staining
C
PMNs + pksP conidia, % Viable
PMNs + wt conidia, % Viable
pksP, APB counts
wt, APB counts
% Viable PMNs
APBs counts x 10³
Time (min)
B
Light scattering (RU)
Size (nm)
2h sEVs
2h wt EVs
2h pksP EVs
3h pksP EVs
3h wt EVs
3h sEVs
4h sEVs
4h pksP EVs
4h wt EVs
D
Relative Opsonization
wt Ab Control
pksP Ab Control
wt
pksP

Figure S3

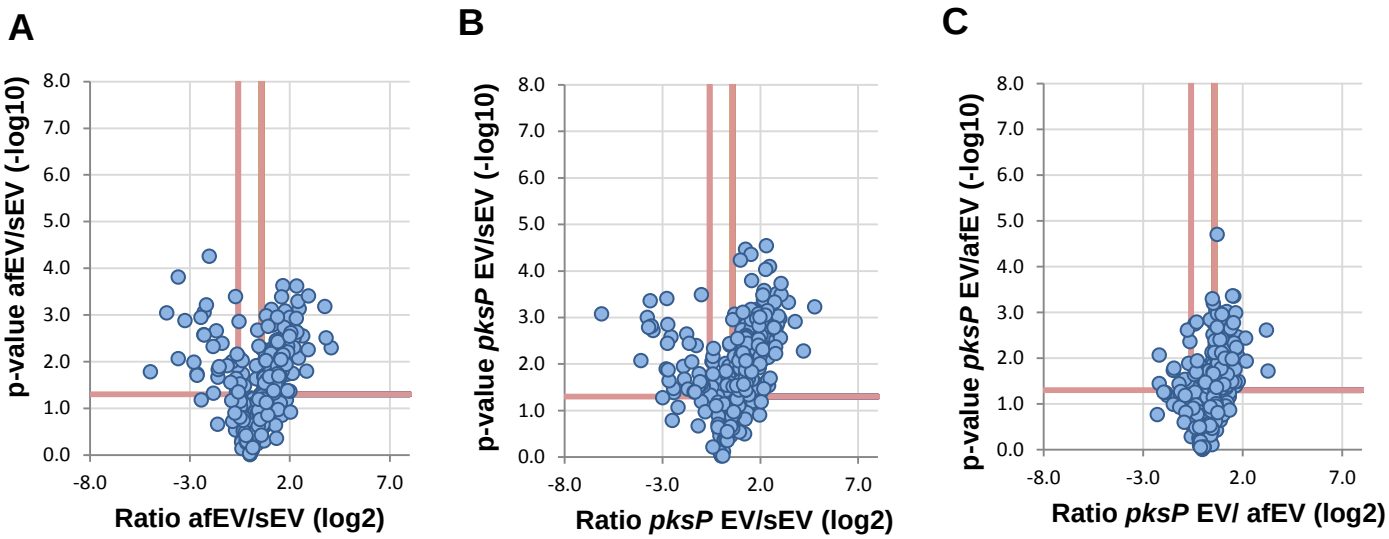
A
B
C
p-value afEV/sEV (-log10)
Ratio afEV/sEV (log2)
p-value pksP EV/sEV (-log10)
Ratio pksP EV/sEV (log2)
p-value pksP EV/afEV (-log10)
Ratio pksP EV/ afEV (log2)
8.0
7.0
6.0
5.0
4.0
3.0
2.0
1.0
0.0
-8.0
-3.0
2.0
7.0

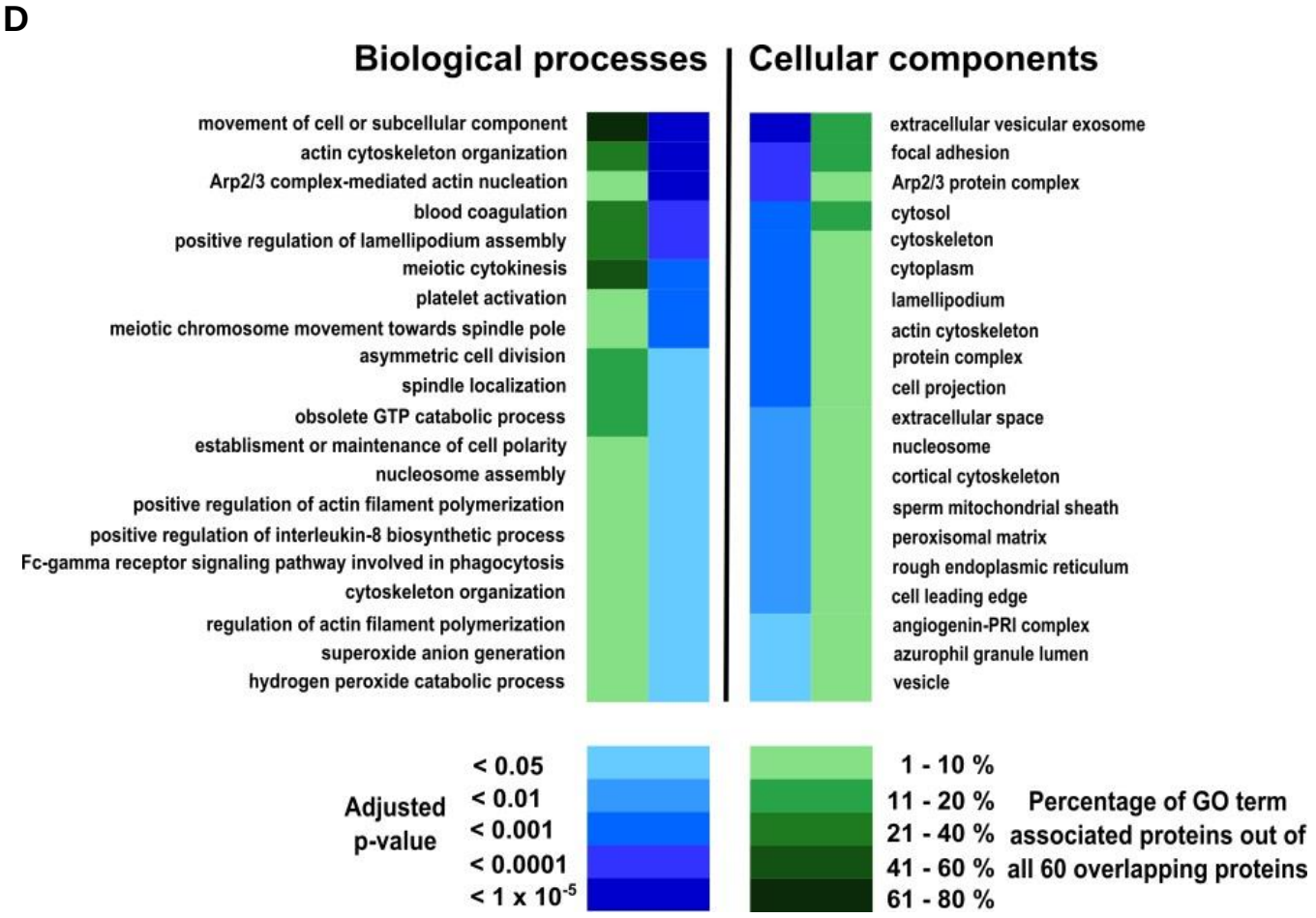
D
Biological processes
Cellular components
movement of cell or subcellular component
actin cytoskeleton organization
Arp2/3 complex-mediated actin nucleation
blood coagulation
positive regulation of lamellipodium assembly
meiotic cytokinesis
platelet activation
meiotic chromosome movement towards spindle pole
asymmetric cell division
spindle localization
obsolete GTP catabolic process
establisment or maintenance of cell polarity
nucleosome assembly
positive regulation of actin filament polymerization
positive regulation of interleukin-8 biosynthetic process
Fc-gamma receptor signaling pathway involved in phagocytosis
cytoskeleton organization
regulation of actin filament polymerization
superoxide anion generation
hydrogen peroxide catabolic process
extracellular vesicular exosome
focal adhesion
Arp2/3 protein complex
cytosol
cytoskeleton
cytoplasm
lamellipodium
actin cytoskeleton
protein complex
cell projection
extracellular space
nucleosome
cortical cytoskeleton
sperm mitochondrial sheath
peroxisomal matrix
rough endoplasmic reticulum
cell leading edge
angiogenin-PRI complex
azurophil granule lumen
vesicle
Adjusted p-value
< 0.05
< 0.01
< 0.001
< 0.0001
< 1 x 10-5
1 - 10 %
11 - 20 %
21 - 40 %
41 - 60 %
61 - 80 %
Percentage of GO term associated proteins out of all 60 overlapping proteins

Figure S4

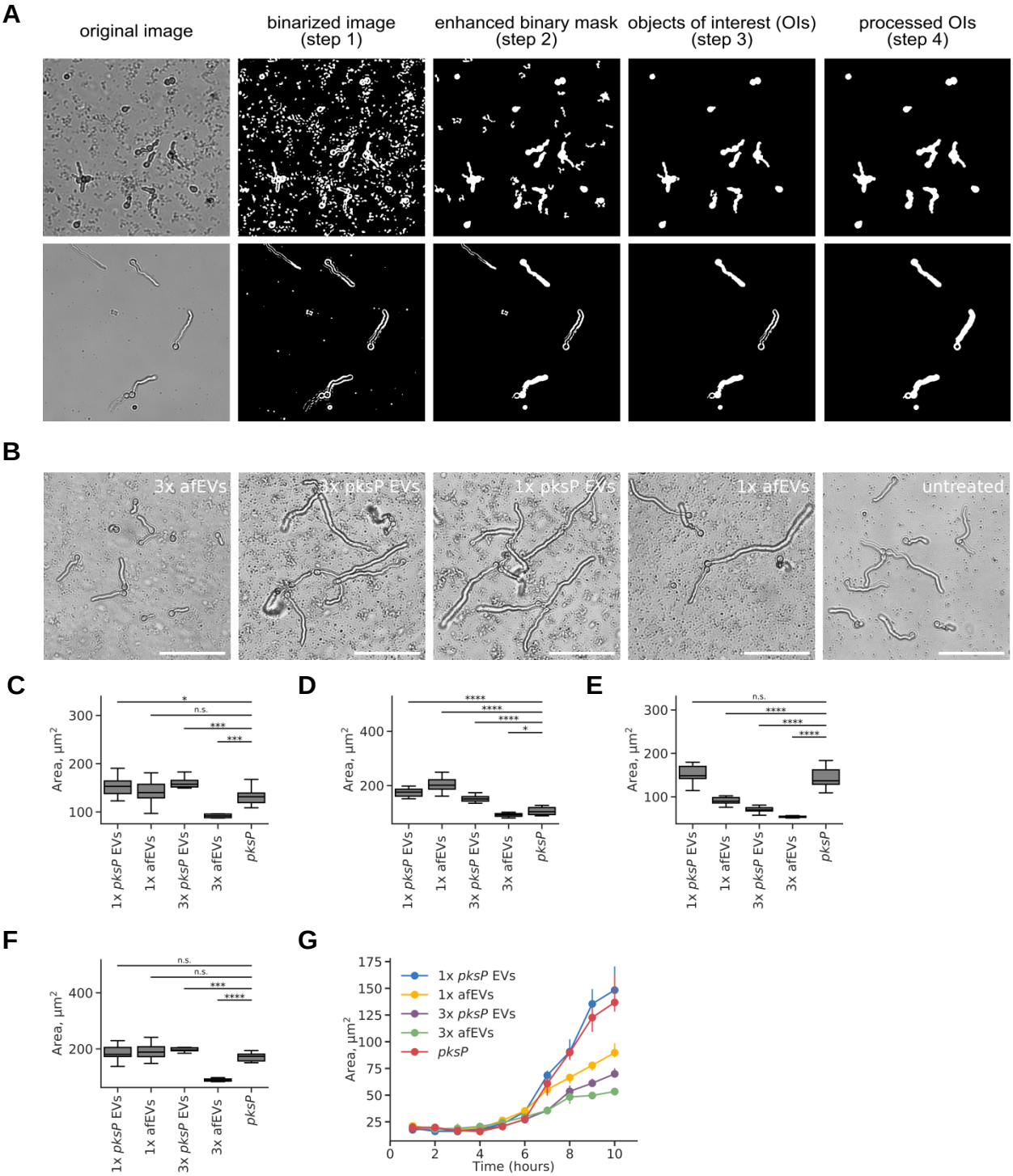
A
original image
binarized image (step 1)
enhanced binary mask (step 2)
objects of interest (OIs) (step 3)
processed OIs (step 4)
B
3x afEVs
3x pksP EVs
1x pksP EVs
1x afEVs
untreated
C
D
E
F
G
Area, µm²
1x pksP EVs
1x afEVs
3x pksP EVs
3x afEVs
pksP
n.s.
Time (hours)

Figure S5

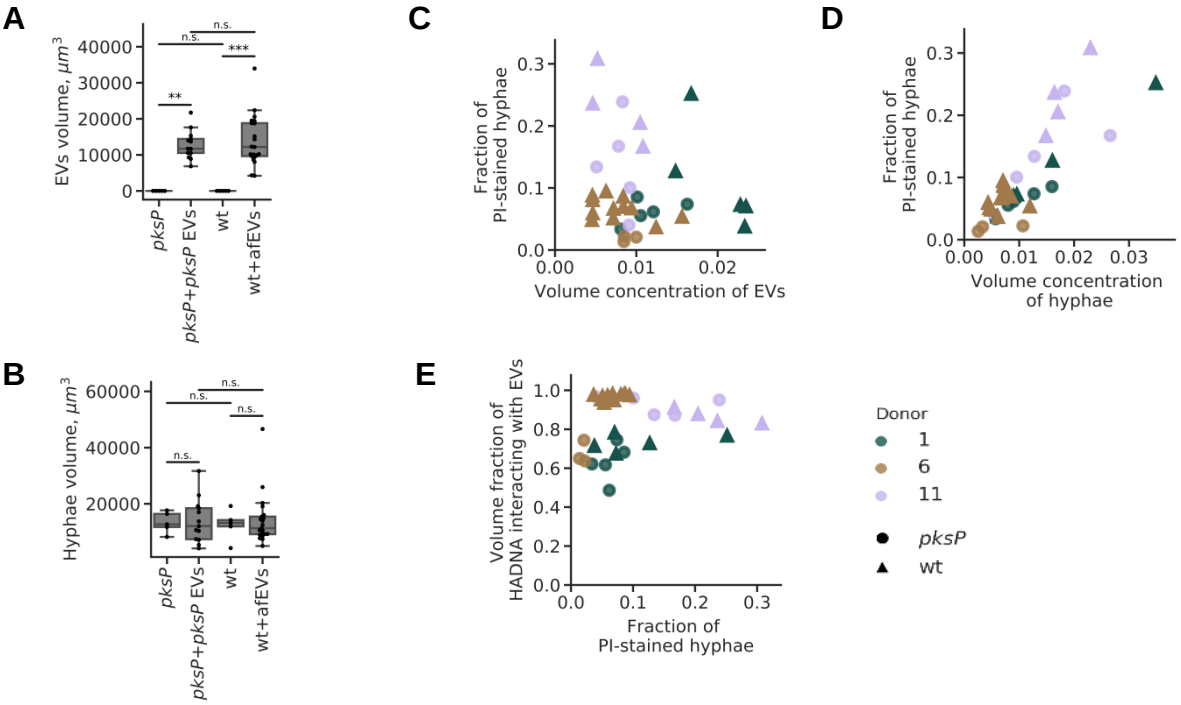
A
EVs volume, μm^3
40000
30000
20000
10000
0
n.s.
n.s.
***
**
pksP
pksP+pksP EVs
wt
wt+afEVs
B
Hyphae volume, μm^3
60000
40000
20000
n.s.
n.s.
n.s.
n.s.
pksP
pksP+pksP EVs
wt
wt+afEVs
C
Fraction of PI-stained hyphae
0.3
0.2
0.1
0.0
0.00
0.01
0.02
Volume concentration of EVs
D
Fraction of PI-stained hyphae
0.3
0.2
0.1
0.0
0.00
0.01
0.02
0.03
Volume concentration of hyphae
E
Volume fraction of HADNA interacting with EVs
1.0
0.8
0.6
0.4
0.2
0.0
0.0
0.1
0.2
0.3
Fraction of PI-stained hyphae
Donor
1
6
11
pksP
wt

Figure S6

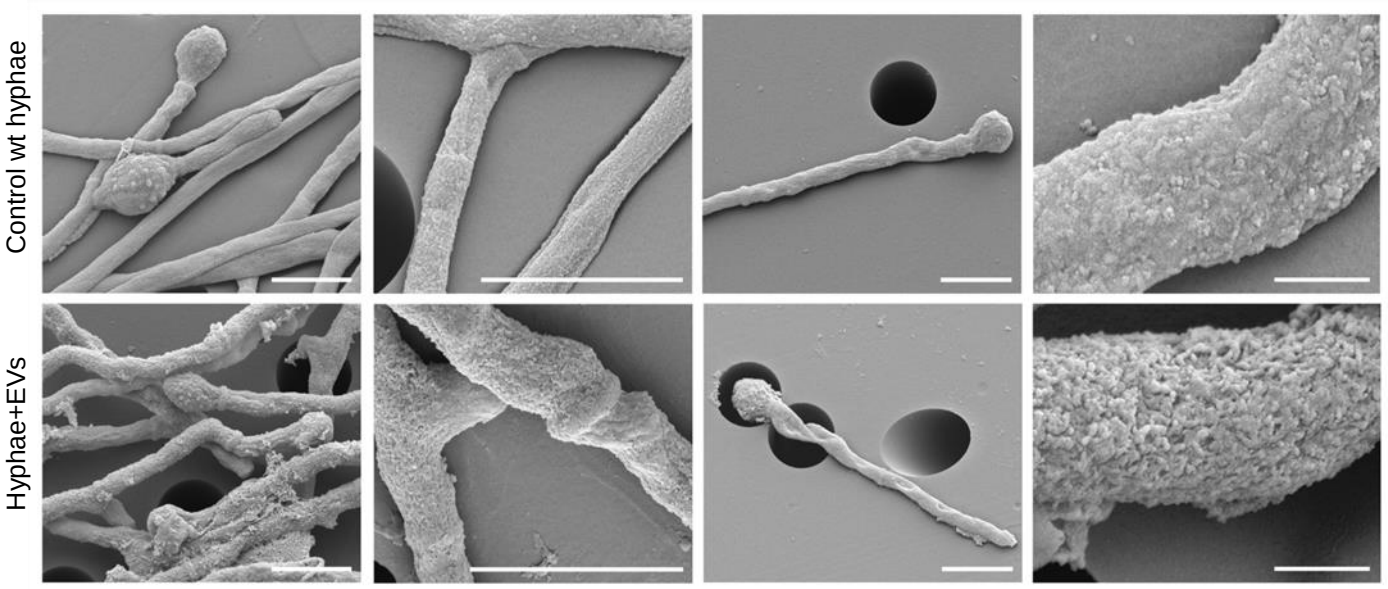

Figure S7

A

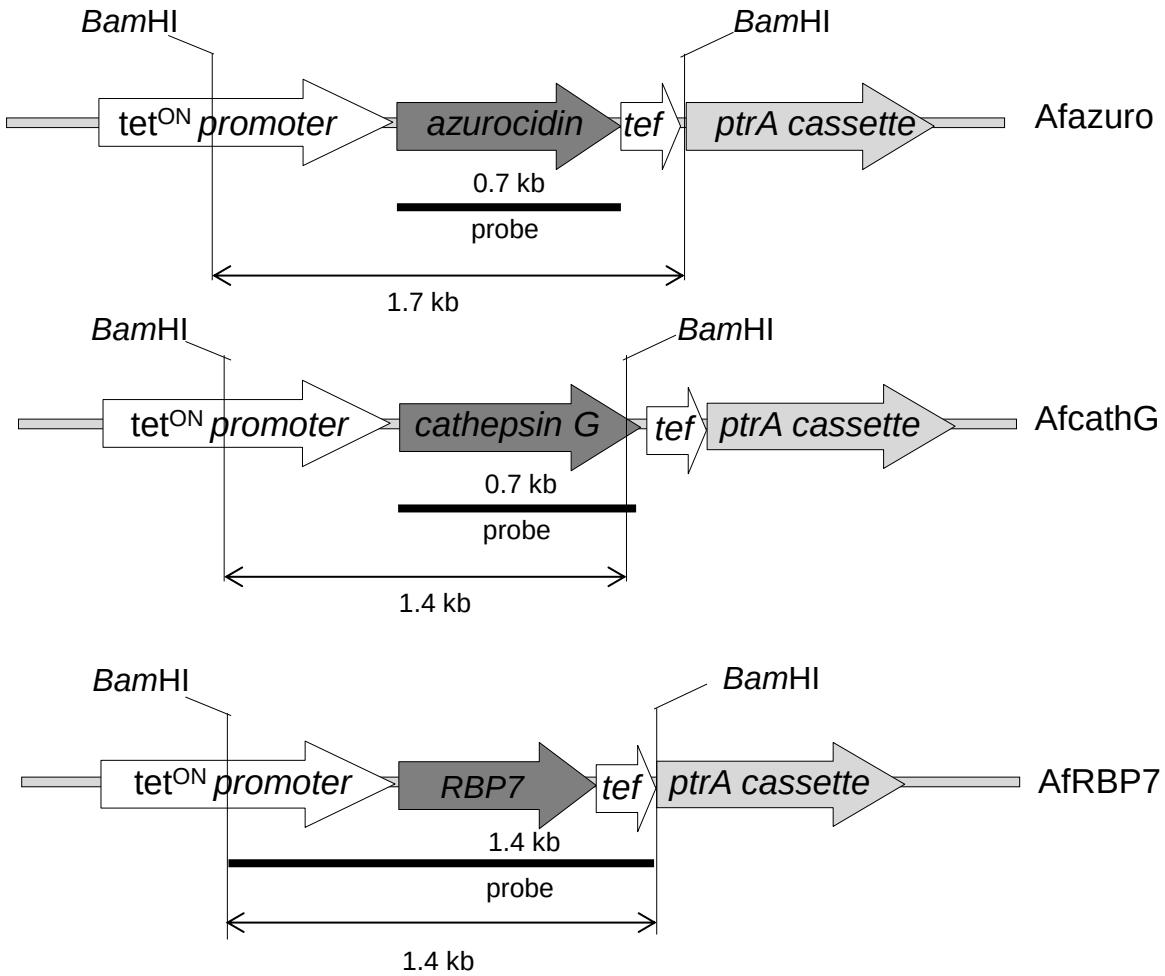
BamHI
BamHI
tetON promoter
azurocidin
tef
ptrA cassette
Afazuro
0.7 kb
probe
1.7 kb
BamHI
BamHI
tetON promoter
cathepsin G
tef
ptrA cassette
AfcathG
0.7 kb
probe
1.4 kb
BamHI
BamHI
tetON promoter
RBP7
tef
ptrA cassette
AfRBP7
1.4 kb
probe
1.4 kb

B

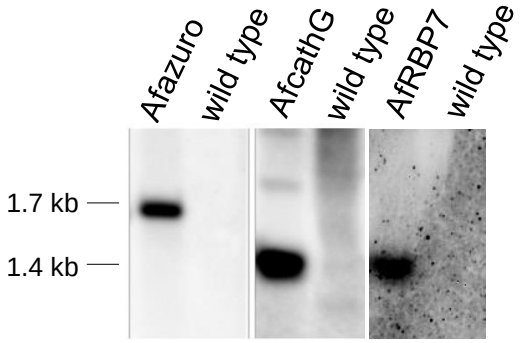
Afazuro
wild type
AfcathG
wild type
AfRBP7
wild type
1.7 kb
1.4 kb

Movies S1 Movie generation by using different dyes and reconstruction

Movie S2 afEVs localize to four regions including the fungal cell wall and cytoplasm

Movie S3 Hyphae respond to afEVs by hyperbranching away from afEVs

S1 Movie. Movie generation by using different dyes and reconstruction. The video shows 3D surface reconstructions for image-based analysis of the interaction of afEVs with *A. fumigatus*. CLSM Z-stacks were captured 20 h post interaction. Cell wall chitin structures were stained with calcofluor white (blue channel). DNA was stained with PI (red channel). afEVs were stained with Annexin-V-FITC (green channel).

S2 Movie. afEVs localize to four regions including the fungal cell wall and cytoplasm The video shows 3D surface reconstructions for image-based analysis of the interaction of afEVs with *A. fumigatus*. CLSM Z-stacks were captured 20 h post interaction. Cell wall chitin structures were stained with calcofluor white (blue channel). afEVs were stained with with Annexin-V Alexa 647 (red channel). The fungal cytoplasm contained eGFP (green channel).

S3 Movie. Hyphae respond to afEVs by hyperbranching away from afEVs The video shows 3D surface reconstructions for image-based analysis of the interaction of afEVs with *A. fumigatus*. CLSM Z-stacks were captured 20 h post interaction. Cell wall chitin structures were stained with calcofluor white (blue channel). DNA was stained with PI (red channel). afEVs were stained with Annexin-V-FITC (green channel).

TABLE S1. Proteins identified with predicted transmembrane domains.

Accession	Protein	TMT dataset	LFQ dataset
P25024	C-X-C chemokine receptor type 1 (CXC-R1)	+	-
P25025	C-X-C chemokine receptor type 2 (CXC-R2)	+	-
Q9HDC9	Adipocyte plasma membrane-associated protein	+	+
P19397	Leukocyte surface antigen CD53	+	-
Q13724	Mannosyl-oligosaccharide glucosidase	+	-
J3KNB4	Cathelicidin antimicrobial peptide	+	-
P15144	Aminopeptidase N	+	+
Q14697	Neutral alpha-glucosidase AB	+	+
P08246	Neutrophil elastase	+	+
M9MML0	Fc of IgG low affinity IIIa receptor isoform 1	+	-
Q8TDB8	Solute carrier family 2, facilitated Glc transporter member 14	+	+
P27105	Erythrocyte band 7 integral membrane protein	+	+
P13498	Cytochrome b-245 light chain	+	+
P08962	CD63 antigen (Granulophysin)	+	-
P04839	Cytochrome b-245 heavy chain	+	-
P17213	Bactericidal permeability-increasing protein (BPI)	+	-
J3KPA1	Cysteine-rich secretory protein 3 CRISP3	+	+
Q53GQ0	Very-long-chain 3-oxoacyl-CoA reductase	-	+
Q96N66	Lysophospholipid acyltransferase 7 (LPLAT 7)	-	+
Q9NV96	Cell cycle control protein 50A	-	+
P08473	Neprilysin	-	+
O43760	Synaptogyrin-2	-	+
P07686	Beta-hexosaminidase subunit beta	-	+
P20701	Integrin alpha-L (CD11 antigen-like family member A)	-	+
F5H2F4	C-1-tetrahydrofolate synthase	-	+
P39656	Dolichyl-diphosphooligosaccharide-protein glycosyltransferase 48 kDa subunit	-	+
P00403	Cytochrome c oxidase subunit 2	-	+
P33121	Long-chain-fatty-acid--CoA ligase 1	-	+
Q15722	Leukotriene B4 receptor 1 (LTB4-R 1)	-	+
I3L0A0	HCG2044781	-	+
Q9NYU2	UDP-glucose:glycoprotein glucosyltransferase 1	-	+
Q8IWA5	Choline transporter-like protein 2	-	+
P13473	Lysosome-associated membrane glycoprotein 2 (LAMP-2)	-	+
Q7L5N7	Lysophosphatidylcholine acyltransferase 2	-	+
O75477	Erlin-1 (Endoplasmic reticulum lipid raft-associated protein 1)	-	+
P21730	C5a anaphylatoxin chemotactic receptor 1	-	+
E7ER45	Maltase-glucoamylase	-	+
P57088	Transmembrane protein 33	-	+

TABLE S2. Twenty most abundant proteins by tandem mass tag quantitation

Accession	Description	PSMs	AAs	PSMs/AAs
P05109	Protein S100-A8	5442	93	58.5
P06702	Protein S100-A9	4808	114	42.2
P80511	Protein S100-A12	992	92	10.8
C9JZR7	Actin, cytoplasmic 1 (Fragment)	913	103	8.9
P02788	Lactotransferrin	5929	710	8.4
P06899	Histone H2B type 1-J	912	126	7.2
P68871	Hemoglobin subunit beta	1039	147	7.1
P59665	Neutrophil defensin 1	650	94	6.9
P60709	Actin, cytoplasmic 1	2275	375	6.1
U3KQK0	Histone H2B	946	166	5.7
P07737	Profilin-1	767	140	5.4
P62736	Actin, aortic smooth muscle	1716	377	4.6
P62805	Histone H4	467	103	4.5
P08311	Cathepsin G	1155	255	4.5
P02042	Hemoglobin subunit delta	600	147	4.1
P04083	Annexin A1	1117	346	3.2
P05164-3	Isoform H7 of Myeloperoxidase	2324	777	3.0
P08246	Neutrophil elastase	752	267	2.8
P69905	Hemoglobin subunit alpha	367	142	2.6
P12429	Annexin A3	773	323	2.4

TABLE S3. Twenty most abundant proteins by label-free quantitation

Accession	Description	PSMs	AAs	PSMs/AAs
P06702	Protein S100-A9	3526	114	30.9
P05109	Protein S100-A8	2704	93	29.1
P59665	Neutrophil defensin 1	2710	94	28.8
P02788	Lactotransferrin	8015	710	11.3
P62805	Histone H4	920	103	8.9
P60709	Actin, cytoplasmic 1	2579	375	6.9
P68871	Hemoglobin subunit beta	940	147	6.4
P08311	Cathepsin G	1463	255	5.7
P68032	Actin, alpha cardiac muscle 1	2045	377	5.4
P69905	Hemoglobin subunit alpha	697	142	4.9
P05164-3	Isoform H7 of myeloperoxidase	3603	777	4.6
G3V1N2	HCG1745306, isoform CRA_a	435	110	4.0
P12429	Annexin A3	1222	323	3.8
P04083	Annexin A1	1175	346	3.4
P02042	Hemoglobin subunit delta	466	147	3.2
P07737	Profilin-1	425	140	3.0
P61626	Lysozyme C	385	148	2.6
Q562R1	Beta-actin-like protein 2	961	376	2.6
P20160	Azurocidin	640	251	2.5
X6R8F3	Neutrophil gelatinase-associated lipocalin	491	200	2.5

TABLE S4. List of primers used in this study.

Name	Sequence (5’-3’)
Azu_polictail_f	TCACCTCCATCTCAACTCCATCACATCACAATGATCGTCGGCGGCCGCAA
cathG_polictail_f	TCACCTCCATCTCAACTCCATCACATCACAATGATCATCGGCGGCCGCGA
RBP7_polictail_F	TCACCTCCATCTCAACTCCATCACATCACAATGCCCGCAGATCTATCTGG
tef_r	ATTAAGGGTTCTCGAGAGCT
pYES2_r	AATATTCCCTATAGTGAGTC
pYES2_f	CTAGAGGGCCGCATCATGTA
ptetOn_pYES2tail_f	GCTGTAATACGACTCACTATAGGGAATATTTCTTTGCCCGGTGTATGAAA
pOliC_r	CTCAACTCCATCACATCACA
ptrA_teftail_f	GTCGAAAACGAGCTCTCGAGAACCCTTAATCAATTGATTACGGGATCCCA
ptrA_pYES2tail_r	CATAACTAATTACATGATGCGGCCCTCTAGTCTTTCTTGTTACACATAAT